



Waterproof molecular monolayers stabilize 2D materials

Cong Su^{a,b,1}, Zongyou Yin^{c,1,2}, Qing-Bo Yan^{a,d,1}, Zegao Wang^{e,f}, Hongtao Lin^{g,h}, Lei Sunⁱ, Wenshuo Xu^j, Tetsuya Yamada^k, Xiang Ji^b, Nobuyuki Zettsu^k, Katsuya Teshima^k, Jamie H. Warner^l, Mircea Dincăⁱ, Juejun Hu^g, Mingdong Dong^e, Gang Su^l, Jing Kong^{b,m}, and Ju Li^{a,g,2}

^aDepartment of Nuclear Science and Engineering, Massachusetts Institute of Technology, Cambridge, MA 02139; ^bResearch Lab of Electronics, Massachusetts Institute of Technology, Cambridge, MA 02139; ^cResearch School of Chemistry, The Australian National University, ACT 2601, Australia; ^dCollege of Materials Science and Opto-Electronic Technology, University of Chinese Academy of Sciences, 100049 Beijing, China; ^eInterdisciplinary Nanoscience Center, Aarhus University, 8000 Aarhus, Denmark; ^fCollege of Materials Science and Engineering, Sichuan University, 610065 Chengdu, China; ^gDepartment of Materials Science and Engineering, Massachusetts Institute of Technology, Cambridge, MA 02139; ^hCollege of Information Science & Electronic Engineering, Zhejiang University, 310027 Hangzhou, China; ⁱDepartment of Chemistry, Massachusetts Institute of Technology, Cambridge, MA 02139; ^jDepartment of Materials, University of Oxford, OX1 3PH, United Kingdom; ^kCenter for Energy and Environmental Science, Shinshu University, 380-8553 Nagano, Japan; ^lSchool of Physical Science, University of Chinese Academy of Sciences, 100049 Beijing, China; and ^mDepartment of Electrical Engineering and Computer Science, Massachusetts Institute of Technology, Cambridge, MA 02139

Edited by Michael L. Klein, Temple University, Philadelphia, PA, and approved September 11, 2019 (received for review June 4, 2019)

Two-dimensional van der Waals materials have rich and unique functional properties, but many are susceptible to corrosion under ambient conditions. Here we show that linear alkylamines $n\text{-C}_m\text{H}_{2m+1}\text{NH}_2$, with $m = 4$ through 11, are highly effective in protecting the optoelectronic properties of these materials, such as black phosphorus (BP) and transition-metal dichalcogenides (TMDs: WS_2 , $1\text{T}'\text{-MoTe}_2$, WTe_2 , WSe_2 , TaS_2 , and NbSe_2). As a representative example, n -hexylamine ($m = 6$) can be applied in the form of thin molecular monolayers on BP flakes with less than 2-nm thickness and can prolong BP's lifetime from a few hours to several weeks and even months in ambient environments. Characterizations combined with our theoretical analysis show that the thin monolayers selectively sift out water molecules, forming a drying layer to achieve the passivation of the protected 2D materials. The monolayer coating is also stable in air, H_2 annealing, and organic solvents, but can be removed by certain organic acids.

molecular monolayer stabilizer | multilayer 2D materials | anticorrosion

Passivation of materials in air and water is foundational to our civilization (1). When we consider the robust ultrathin passivation of 2D materials (2–7), it should be even more essential because 1) the thickness of passivation layer on 3D materials like Si, Al, Cr, etc. stays 2 to 5 nm over a very long time, which is an insignificant fraction of the remaining unreacted bulk material. However, one cannot say this for thin 2D materials with their total thickness likely comparable to the native oxide passivation layers. Thus, the atomistic details of passivation matter even more here. 2) An ultrathin, electronically insulating layer provides opportunity to engineer extremely thin vertical heterostructures, akin to the SiO_2/Si gate in metal-oxide-semiconductor field-effect transistors. For these reasons, it is becoming increasingly critical to facily passivate layered materials such as transition-metal dichalcogenides (TMDs), black phosphorus (BP), silicene, stanine (8–12), etc., which are susceptible to corrosion under ambient conditions with air, water, or even small amounts of acidic or basic contaminants (9, 10, 13–19).

Several passivation strategies have been developed for these layered materials including covering by more robust 2D materials such as graphene (20) and hexagonal boron nitride (21). However, many previous strategies suffer from processability issues and other drawbacks: Metal-oxide coatings are prone to cracking (14, 22); polymers [e.g., poly(methyl methacrylate) (PMMA), polystyrene, Parylene, and perylene-3,4,9,10-tetracarboxylic dianhydride] are readily attacked by organic solvents and offer limited durability (19, 23–26); self-assembled monolayers with silane-terminated octadecyltrichlorosilane are highly toxic (27). Here, we discovered a one-pot scalable process for passivating a large variety of 2D van

der Waals materials. It involves coating a nanometer-thick monolayer of linear alkylamines onto the surface of 2D materials, which greatly increases the lifetime of these materials in ambient environments with moisture and can sustain even harsh aqueous and thermal conditions. First-principles simulations suggest that the alkylamine coating significantly slows down the permeation of O_2 , which reacts with the 2D layered material to form an ultrathin oxide passivation layer, and completely blocks H_2O molecules and shuts down the cycles of oxidation–dissolution, leading to the extended lifetime for many different classes of 2D crystals.

Since BP is the most vulnerable to corrosion among the 2D van der Waals (vdW) materials studied in this work and creates the most challenges for processing, it is used here as an illustrative example of the alkylamine coating. As a representative example of linear alkylamines $n\text{-C}_m\text{H}_{2m+1}\text{NH}_2$, n -hexylamine ($m = 6$) coating onto BP is systematically investigated both theoretically and experimentally in its corrosion inhibition mechanism and behaviors.

Results

The coating process is divided into 2 steps: 1) The sample together with silicon substrate is put in the liquid n -hexylamine for 20 min under 130 °C. This step creates coating on sample, but minor cracks might exist. 2) To fix the cracks, the sample is then immersed in hexylamine vapor for another 20 min at 130 °C and then annealed in argon for 30 min under 200 °C after the surface

Significance

A family of strong yet removable 1- to 2-nm-thick ultrathin monolayer is developed as a corrosion inhibitor for 2-dimensional materials that significantly prolong lifetime while protecting optoelectronic properties in both ambient and harsh chemical or thermal environments. This method is low in toxicity and can be applied to arbitrary substrate with no size limit.

Author contributions: C.S., Z.Y., and J.L. designed research; C.S., Z.Y., Q.-B.Y., Z.W., H.L., W.X., T.Y., and X.J. performed research; C.S., Z.Y., L.S., N.Z., K.T., J.H.W., M. Dincă, J.H., M. Dong, G.S., J.K., and J.L. analyzed data; N.Z., K.T., J.H.W., M. Dincă, J.H., M. Dong, G.S., J.K., and J.L. supervised the project; and C.S., Z.Y., and J.L. wrote the paper.

Competing interest statement: US Patent under International Application PCT/US2018/025174 has been filed for technique related to this work.

This article is a PNAS Direct Submission.

Published under the PNAS license.

¹C.S., Z.Y., and Q.-B.Y. contributed equally to this work.

²To whom correspondence may be addressed. Email: Zongyou.yin@anu.edu.au or liju@mit.edu.

This article contains supporting information online at www.pnas.org/lookup/suppl/doi:10.1073/pnas.1909500116/-DCSupplemental.

First published October 1, 2019.

is cleaned by hexane. The hexane cannot remove the hexylamine coating but only the surface contamination, as shown later. More detailed coating procedures are presented in *SI Appendix, Fig. S1* (28–40). The optimization of coating parameters of *n*-hexylamine onto BP is shown in *SI Appendix, Table S1*.

Once mechanically exfoliated, the bare BP flakes are highly reactive and chemically unstable. After keeping a 3-nm-thick BP flake in ambient air (humidity $\sim 35\%$) for 2 d (the thickness is estimated using the method from ref. 9), only vague traces remain (Fig. 1A), even when care is taken to prevent light exposure, known to accelerate the damage. As shown in Fig. 1A, the 3 characteristic Raman peaks of BP at 361 cm^{-1} (A_g^1), 438 cm^{-1} (B_{2g}), and 466 cm^{-1} (A_g^2) completely disappear after 2 d. The degradation of BP is further expedited when exposed to light, in line with previous reports (9) which showed that the lifetime of BP (defined as the time needed for the Raman intensity to drop to e^{-1} of its original) is $\tau \sim 1\text{ h}$ when a 2.8-nm-thick sample is exposed to a photon flux of $1.8 \times 10^3\text{ W/cm}^2$, and $\tau \sim 10\text{ min}$ when exposed to a photon flux of $1.7 \times 10^4\text{ W/cm}^2$.

In contrast, *n*-hexylamine protected BP (HA-BP hereafter), which is kept side-by-side with the unprotected one, exhibits robust BP characteristics for a much-extended period. The difference in optical contrast for HA-BP between 0 and 111 d is essentially indiscernible (Fig. 1B); 31% of the intensity of A_g^2 was retained after 111 d. The photon fluence seen by HA-BP during Raman measurements in 111 d is equivalent to light

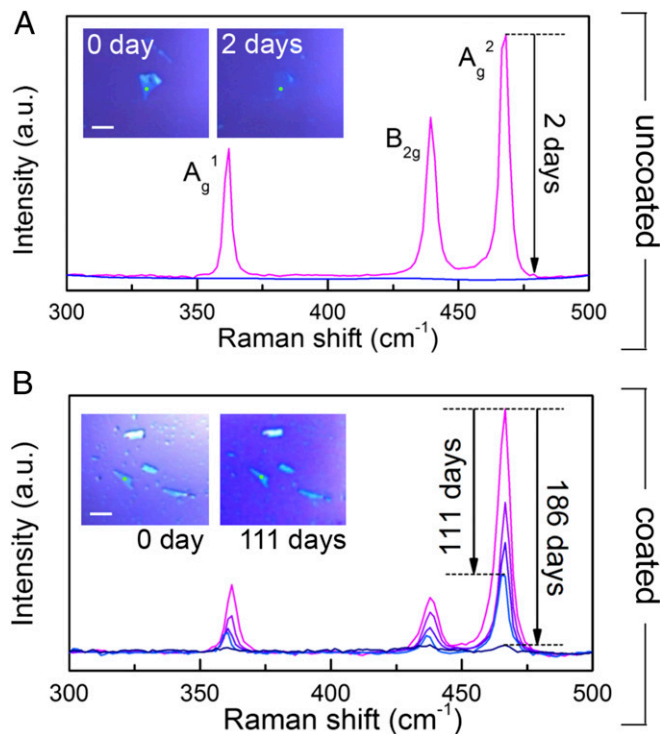


Fig. 1. Comparison of BP flakes with and without *n*-hexylamine coating. (A) The Raman spectra at $\lambda = 532\text{ nm}$ of the bare BP flake. (Insets) Optical images of the exfoliated BP flake on SiO_2/Si wafer before aging (on 0 d), and after 2-d aging in ambient conditions where only the blurry marks of original flake could be identified. (B) The corresponding Raman spectra of the *n*-hexylamine-coated sample on the 0, 13, 41, 111, and 186 d. (Insets) Optical images of *n*-hexylamine-coated BP flakes on SiO_2/Si before aging (on 0 d), and after 111-d aging under the same ambient conditions. (Insets) Green dots are laser spot positions for repeated spectra acquisition. All samples are dried for 30 min at 120°C in air right after being prepared. All Raman spectra shown above have been renormalized and calibrated to Si (reference) peak intensity. (Scale bars, $5\ \mu\text{m}$.)

exposure of $1.0 \times 10^5\text{ W/cm}^2$ for $\sim 2\text{ h}$ in total. Since such photon exposure is already known to be substantial to cause the degradation of bare BP (ref. 9), we conclude that the lifetime of HA-BP can be extended even further if the sample has not been exposed to the laser beam of the Raman characterization.

The coating process involves the proton transfer of the hydroxylated BP to the $-\text{NH}_2$ group of *n*-hexylamine based on the evidence below. First-principles simulations suggest that *n*-hexylamine forms a molecular monolayer as shown in Fig. 2A. The top layer of the BP surface is rapidly oxidized from the oxygen dissolved in liquid hexylamine, forming P–OH, P–O $^-$, or P=O surface groups. Experimental evidence supports a model where the acidic P–OH groups on the BP surface and the terminal $-\text{NH}_2$ groups of alkylamines undergo a Brønsted–Lowry acid–base reaction to form a layer of alkylammonium salts that coat the BP surface through a strong electrostatic interaction with the deprotonated P–O $^-$ surface sites. Confirmation that the neutral $-\text{NH}_2$ group in *n*-hexylamine becomes charged (i.e., $-\text{NH}_3^+$) came from X-ray photoelectron spectroscopy (XPS): Comparing the N 1s peaks between HA-BP, dodecylamine ($\text{C}_{12}\text{H}_{25}\text{NH}_2$, R– NH_2), and methylammonium chloride ($\text{CH}_3\text{NH}_3\text{Cl}$, R– NH_3^+) reveals that HA-BP and R– NH_3^+ have the same binding energy, which is blueshifted by 2.4 eV from that of R– NH_2 (Fig. 2B). Contact-angle measurements also show that the surface of BP becomes more hydrophobic after HA coating (*SI Appendix, Fig. S2*), confirming that the HA coating is indeed terminated by alkyl chains, not by amine/ammonium groups.

Inspection by atomic force microscopy (AFM) of the height profile of the same 2D flake before and after coating revealed that the *n*-hexylamine coating is around 1.5 nm thick (Fig. 2C), which is consistent with the theoretical chain length of *n*-hexylamine (41). This demonstrates that the deposition of *n*-hexylamine molecules is self-limiting. Polar organic solvents including acetone, ethanol, or isopropanol, as well as nonpolar solvents like hexane, cannot remove the *n*-hexylamine coating, indicating that the interaction between *n*-hexylamine and BP is strong enough to sustain solvent attack. We also note that *n*-hexane does not impart any corrosion protection, attesting that the amine group is key for this function and that the alkyl chain itself cannot bind strongly on BP.

We employed first-principles calculations to investigate the transfer of protons when *n*-hexylamine approaches P–OH (Fig. 2D), formed by reacting with the water from the *n*-hexylamine coating solution. Among various structural possibilities after systematic study, with results shown in *SI Appendix, Figs. S3–S6*, the most likely reaction pathway agrees with the scenario (P–O $^-$ – NH_3^+ – C_6H_{13}) proposed above and yields a bonding energy of 0.97 eV, which is 3 to 4 \times stronger than the pure vdW interaction [$\sim 0.33\text{ eV}$ between *n*-hexylamine and pure BP, $\sim 0.22\text{ eV}$ between amines and graphene (42)]. The electronic density distribution shows that the H atom shares its orbital much more with N atom than with O atom (Fig. 2D, Inset), and Bader charge analysis indicates that *n*-hexylammonium ($\text{C}_6\text{H}_{13}\text{NH}_3^+$) carries a net charge of $+0.89e$, and to compensate, the rest has $-0.89e$.

In Fig. 2E, the migration energy barrier of H_2O penetrating through *n*-hexylamine is calculated to be 1.4 eV and O_2 1.0 eV, when *n*-hexylamine covers BP in the densest possible packing structure (hereafter defined as 100% coverage, shown in *SI Appendix, Figs. S8 and S9*); when the coverage drops to 66.7%, the migration energy barrier reduces to 0.2 eV for H_2O permeation and no barrier (0 eV) for O_2 . When the HA coverage further decreases to 50% or 25%, the migration of both H_2O and O_2 through the HA layer toward the surface of BP is barrierless. Combining this theoretical analysis with the time-evolution XPS data on phosphorus oxide concentration (Fig. 2F and G), where the oxidation speed of phosphorus after *n*-hexylamine coating is significantly reduced by 32 \times at the beginning of oxidation (fitting method and definition of time constant can be found in

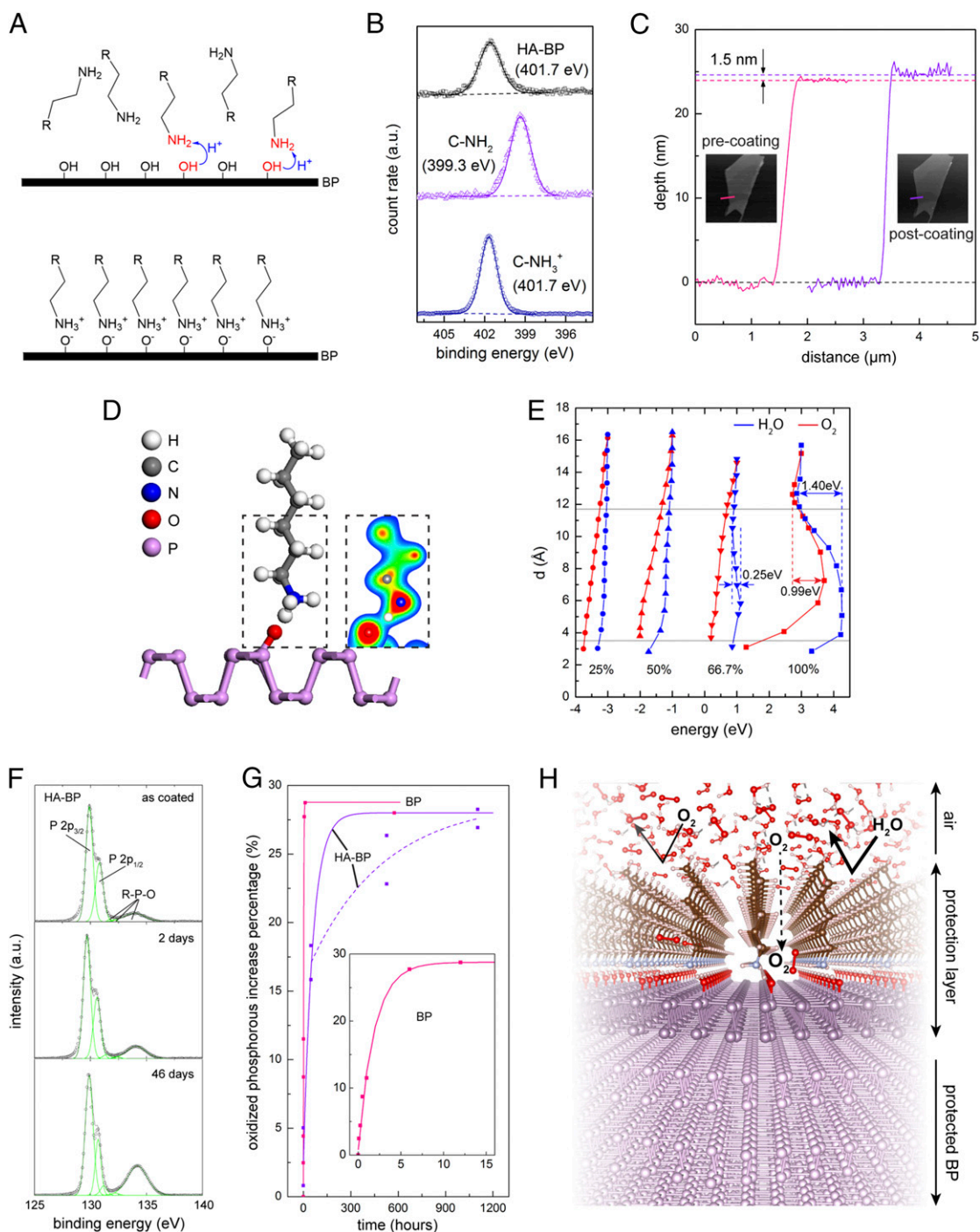


Fig. 2. The mechanism of *n*-hexylamine coating on BP. (A) Proton transfer takes place during the coating process (*Upper*) and the *n*-hexylamine monolayer is formed on BP after the coating process is done (*Lower*). R- in the diagram refers to C_4H_9 - when representing hexylamine. (B) XPS spectra of nitrogen 1s peaks on HA-BP, dodecylamine (C-NH₂), and CH₃NH₃Cl (C-NH₃⁺), proving that the amino group of *n*-hexylamine coated on BP is in ionic state -NH₃⁺. (C) The AFM data revealing the thickness of a BP flake with 24 nm before coating (pink line) and the thickness increment after hexylamine coating (violet line). (D) The schematic structure of *n*-hexylamine adsorbed on BP, where red-, blue-, purple-, and white-colored balls represent oxygen, nitrogen, carbon, phosphorus, and hydrogen, respectively. (*Inset*) the contour map of valence electron density on the plane containing O, N atoms and the H atom between them, which corresponds to the part marked by rectangle dashed line. (E) The energy profile of H₂O and O₂ molecules when penetrating through the hexylamine molecule layer. The y axis is the distance between the bottom atom of H₂O or O₂ and the surface of BP, denoted as *d*. Blue and red curves represent H₂O and O₂ penetration processes, respectively. The 4 groups of curves represent different coverages of 25, 50, 66.7, and 100% (detailed coverage definition illustrated in *SI Appendix, Fig. S7*), as marked. The horizontal gray lines are the locations of the top and the bottom of hexylamine molecules. (F) The P 2p peaks and oxidized phosphorus species (R-P-O) of XPS curves on HA-BP measured as coated, after 2 d, and after 46 d. (G) The phosphorus oxide concentration as a function of time between *n*-hexylamine-coated (violet triangles) and uncoated BP samples (pink squares). (*Inset*) A blow-up of the uncoated sample data between 0 and 15 h. Both datasets are fitted with exponential curves. The pink and violet solid lines are fittings of the scattered data pointing to the uncoated and HA-coated samples, respectively. Note that the oxidation of HA-BP is a significant slowdown starting from 100 h, so a second curve fitting is marked (dashed violet line). (H) Schematic illustration of the structure of BP after coating by *n*-hexylamine. The first layer of BP is oxidized and forms a part of protective layer together with the *n*-hexylamine coating. The surface protective layer (hexylammonium + first-layer oxidized BP) protects the rest of BP underneath.

SI Appendix), we deduce the coverage density of *n*-hexylamine on BP must be more than the defined 66.7% coverage on the surface of BP.

With these conclusions, a schematic illustration of the molecular monolayer can be shown in Fig. 2*H*. The top oxidized BP layer of PO_x together with the coated *n*-hexylamine monolayer forms a dense protection layer for the BP underneath. It lowers the penetration speed of O₂ molecule significantly and blocks the H₂O molecule almost completely under room temperature, thus stabilizing the surface passivation layer (the oxidized BP at the top).

The anticorrosion effect conferred by organic monolayer is not limited to *n*-hexylamine. Indeed, other linear alkylamines *n*-C_{*m*}H_{2*m*+1}NH₂ with *m* = 4 through 11, including *n*-butylamine (*n*-C₄H₉NH₂), *n*-pentylamine (*n*-C₅H₁₁NH₂), *n*-octylamine (*n*-C₈H₁₇NH₂), *n*-decylamine (*n*-C₁₀H₂₁NH₂), and *n*-undecylamine (*n*-C₁₁H₂₃NH₂), all consistently displayed similar anticorrosion effects in ambient air. Their coatings onto BP for anticorrosion demonstration are presented in *SI Appendix*, Table S2, and the growth parameters for coating all these alkylamines with different carbon chain lengths are summarized in *SI Appendix*, Table S3.

To demonstrate the passivation efficacy for actual optoelectronic devices in ambient and aggressive environments, we fabricated 2 BP-flakes-based photodetectors. As a direct bandgap semiconductor, with its *E*_{gap} continuously tunable from ~2 eV (single layer) to 0.3 eV (bulk) (43) by varying the number of layers, BP stands out as a promising material for photonic devices from near-infrared to midinfrared. The layout of the uncoated BP detector with a channel length and width of ~3 and ~5 μm, respectively, between the Ti/Au electrodes is shown in Fig. 3*A*. The thickness of the BP here is 74 nm (*SI Appendix*, Fig. S10). The *n*-hexylamine-coated BP photodetector is shown in Fig. 3*B*, with comparable channel dimension and a BP thickness of 55 nm (*SI Appendix*, Fig. S10). Note here, the photocurrent for bare BP device is significantly lower than the protected one due to the fast degradation of BP in air during sample loading and contacting electrical probes. The photocurrent and current density as a function of input optical power under zero voltage bias (Fig. 3*A* and *B*, uncoated and coated respectively) was measured in ambient air with a 1,550-nm laser. The coated BP can sustain annealing in H₂ environment under 250 °C for 1 h, proved by H₂O₂ etching experiment. Both devices exhibited increased photocurrent with input power before etching (black lines labeled with preetching in these plots). After dipping the devices in H₂O₂ for 5 s and drying them subsequently, obvious degradation was observed under optical microscope on the uncoated BP device (Fig. 3*A*, Upper-Right Inset), while little change was found on the coated one (Fig. 3*B*, Upper-Right Inset). As evidenced by the photoelectric signal, corrosion caused severe damage to the uncoated optoelectronic device, with the photocurrent dropping to 0. In contrast, the *n*-hexylamine-coated photodetector device maintained 78.6% of its original photocurrent based on the photocurrent values of 28.7 μA at postetching and 36.5 μA at preetching under photoexcitation with the same input power of 3 mW. The slight drop of performance likely originates from defects in the coating layer within the boundaries between the electrode metal and the BP flake, and also likely originates from the residue of PMMA during the deposition of electrodes that blocks the spreading of hexylamine.

Such monolayer protection is effective not only for BP, but also for other layered 2D materials. Here, to accelerate corrosion tests for *n*-hexylamine-coated 2D materials, we used harsh aqueous H₂O₂ or KMnO₄ solutions as etchants. In Table 1, we take the optical microscopy images during the corrosion exposure for each 2D material, including BP, WS₂, WSe₂, 1T'-MoTe₂, WTe₂, TaS₂, and NbSe₂. It should be noted that exfoliated BP, 1T'-MoTe₂, WTe₂, NbSe₂ and chemical vapor deposition (CVD)-grown single-layer WS₂ are known to be particularly susceptible to

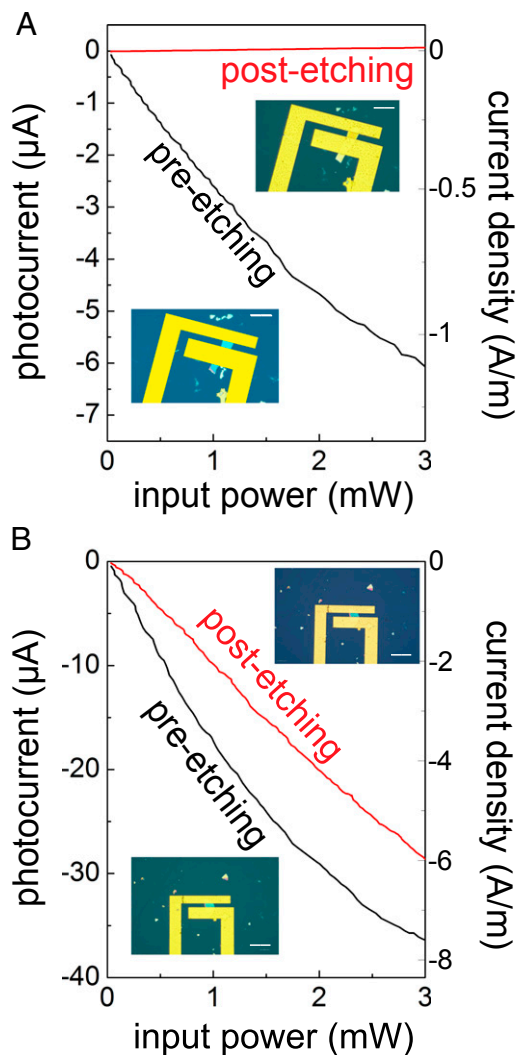


Fig. 3. Photodetectors and etching test. (A) Photocurrent and current density as a function of input optical power under zero bias voltage. (Insets) The optical images of uncoated BP devices before (Bottom Left) and after etching (Top Right) by an aqueous solution of 30 wt % H₂O₂ for 5 s. (B) *n*-hexylamine-coated-device counterparts of A. (Scale bars, 10 μm.)

ambient corrosion and are readily attacked by solutions of H₂O₂. WSe₂ and TaS₂ are less vulnerable and require stronger oxidants for corrosion. *n*-hexylamine is proved to be effective in protecting these layered materials based on the comparison in optical image between uncoated and coated 2D materials after their exposure to the same etchants. A movie of the corrosion retardation for BP is presented as *Movie S1*.

Despite the fact that *n*-hexylamine is sturdy under various environments, it is still removable by certain organic acids. Presumably, the organic-media-supported protons can penetrate the hydrophobic alkyl layer and protonate the ionized surface P-O⁻ groups, disrupting their electrostatic interaction with the alkylammonium cations. This removing protocol is effective both for the amine coating on BP and TMDs, without affecting the passivation oxidized layer and the materials underneath (*SI Appendix*, section 5).

Discussion

Amines with low water solubility have long been known as efficient and reliable corrosion inhibitors for steels (41, 44). It is found here that they also serve as an effective coating for 2D

Table 1. Protection of various 2D materials with *n*-hexylamine coatings

material / etchant with etching time	bare		coated	
	before exposure	after exposure	before exposure	after exposure
BP (exfoliated) / 20sec in H ₂ O ₂ (30 wt. % in H ₂ O)				
WS₂ (CVD, monolayer) / 5sec in H ₂ O ₂ (30 wt. % in H ₂ O)				
1T'-MoTe₂ (exfoliated) / 10sec in H ₂ O ₂ (30 wt. % in H ₂ O)				
WTe₂ (exfoliated) / 30sec in H ₂ O ₂ (30 wt. % in H ₂ O)				
WSe₂ (exfoliated) / 1min in KMnO ₄ (0.02mol/L in H ₂ O)				
TaS₂ (exfoliated) / 1min in KMnO ₄ (0.01mol/L in H ₂ O)				
NbSe₂ (exfoliated) / 20sec in H ₂ O ₂ (30 wt. % in H ₂ O)				

BP, WS₂, 1T'-MoTe₂, WTe₂, WSe₂, TaS₂, and NbSe₂ were coated with *n*-hexylamine and dipped inside etchants of H₂O₂ or KMnO₄ solution (depending on the respective material reactivity) as an accelerated lifetime test. The uncoated counterparts were processed in parallel with the coated parts under identical etching conditions. (Scale bars, 10 μm.)

layered materials, by blocking water for the native thin-oxide layer growing at the interface between the 2D material and the alkylamine coating. The photooxidation of bare BP starts with the synergetic effect of oxygen, water, and light, where phosphorus transformed to a layer of acidic phosphorus species. The thin layer of acid then coarsens into a droplet, leaving a fresh phosphorus surface in contact with ambient air, and the oxidation process starts once again (45). *n*-hexylamine monolayer lowers the permeability of oxygen and strongly blocks the water molecules from directly contacting the oxide passivation layer and phosphorus. Although the first BP layer is still oxidized by O₂, it is isolated from ambient humidity by the hydrophobic alkyl monolayer, which prevents the water from dissolving this top native oxide that would have perpetuated the corrosion. Our experimental finding of the passivation effect on BP is consistent with the theoretical prediction that mere BP + O₂ reaction forming BP-PO_x should be fully stable and self-limiting at ~1 to 2 nm if no moisture exists (31).

In summary, we have developed a strategy to effectively slow down the corrosion of BP by coating of alkylamine monolayer onto its surface. General applicability on a variety of other layered materials is also demonstrated. The alkylamine monolayer is robust in a range of chemical and thermal environments, including ambient air. The facile coating method can be implemented

with many different substrates and is compatible with all linear alkylamines no shorter than *n*-butylamine, thus offering a platform for controlling the surface physics and chemistry of a rich tableau of 2D materials. Because of its simplicity, ecofriendliness, and low cost, we envision it to be scalable and adaptable in various industrial configurations.

ACKNOWLEDGMENTS. C.S. and Z.Y. would like to thank Philip Kim for granting lab access for the glovebox-enclosed AFM. C.S. would like to thank Greg Lin and Frank Zhao for helpful discussions. Z.Y. thanks Pablo Jarillo-Herrero for providing the glovebox. J.L., C.S., M.D. (MIT), and L.S. acknowledge support by the Center for Excitonics, an Energy Frontier Research Center funded by the US Department of Energy, Office of Science, Basic Energy Sciences under Award DE-SC0001088. J.L., C.S., and Z.Y. acknowledge support by NSF ECCS-1610806, the Australian Research Council Discovery Project (Grant DP190100295), and the Australian National University (ANU) Futures Scheme (Grant Q4601024). Q.-B.Y. and G.S. acknowledge support in part by the Ministry of Science and Technology of China (Grant 2013CB933401), the National Science Foundation of China (Grant 11474279), and the Strategic Priority Research Program of the Chinese Academy of Sciences (Grant XDB07010100). H.L. and J.H. acknowledge funding support provided by NSF under Award 1453218. J.H.W. acknowledges the support from the Royal Society. J.K. and C.S. acknowledge support from the US Army Research Office through the Massachusetts Institute of Technology Institute for Soldier Nanotechnologies, under Award O23674. T.Y., N.Z., and K.T. acknowledge support by Inter-University Cooperative Research Program of the Institute for Materials Research, Tohoku University (program no. 15G0031).

- D. D. Macdonald, Passivity—The key to our metals-based civilization. *Pure Appl. Chem.* **71**, 951–978 (1999).
- K. F. Mak, C. Lee, J. Hone, J. Shan, T. F. Heinz, Atomically thin MoS₂: A new direct-gap semiconductor. *Phys. Rev. Lett.* **105**, 136805 (2010).
- H. R. Gutiérrez *et al.*, Extraordinary room-temperature photoluminescence in triangular WS₂ monolayers. *Nano Lett.* **13**, 3447–3454 (2013).
- Y. Zhang *et al.*, Direct observation of the transition from indirect to direct bandgap in atomically thin epitaxial MoSe₂. *Nat. Nanotechnol.* **9**, 111–115 (2014).
- J. S. Ross *et al.*, Electrically tunable excitonic light-emitting diodes based on monolayer WSe₂ p-n junctions. *Nat. Nanotechnol.* **9**, 268–272 (2014).
- X. Qian, J. Liu, L. Fu, J. Li, Quantum spin hall effect in two-dimensional transition metal dichalcogenides. *Science* **346**, 1344–1347 (2013).
- Y. Yu *et al.*, Gate-tunable phase transitions in thin flakes of 1T-TaS₂. *Nat. Nanotechnol.* **10**, 270–276 (2015).
- L. Tao *et al.*, Silicene field-effect transistors operating at room temperature. *Nat. Nanotechnol.* **10**, 227–231 (2015).
- A. Favron *et al.*, Photooxidation and quantum confinement effects in exfoliated black phosphorus. *Nat. Mater.* **14**, 826–832 (2015).
- L. Li *et al.*, Black phosphorus field-effect transistors. *Nat. Nanotechnol.* **9**, 372–377 (2014).
- F. F. Zhu *et al.*, Epitaxial growth of two-dimensional stanene. *Nat. Mater.* **14**, 1020–1025 (2015).
- P. Vishnoi, U. Gupta, R. Pandey, C. N. R. Rao, Stable functionalized phosphorenes with photocatalytic HER activity. *J. Mater. Chem. A* **7**, 6631–6637 (2019).
- A. K. Geim, I. V. Grigorieva, Van der Waals heterostructures. *Nature* **499**, 419–425 (2013).
- J. D. Wood *et al.*, Effective passivation of exfoliated black phosphorus transistors against ambient degradation. *Nano Lett.* **14**, 6964–6970 (2014).
- S. Ross, A. Sussman, Surface oxidation of molybdenum disulfide. *J. Phys. Chem.*, **59**, 889–892 (1955).
- Y. Zhang *et al.*, Controlled growth of high-quality monolayer WS₂ layers on sapphire and imaging its grain boundary. *ACS Nano* **7**, 8963–8971 (2013).
- S. P. Koenig, R. A. Doganov, H. Schmidt, A. H. Castro Neto, B. Özyilmaz, Electric field effect in ultrathin black phosphorus. *Appl. Phys. Lett.* **104**, 103106 (2014).
- A. Castellanos-Gomez *et al.*, Isolation and characterization of few-layer black phosphorus. *2D Mater.* **1**, 025001 (2014).
- J. Gao *et al.*, Aging of transition metal dichalcogenide monolayers. *ACS Nano* **10**, 2628–2635 (2016).
- M. J. Nine, M. A. Cole, D. N. H. Tran, D. Losic, Graphene: A multipurpose material for protective coatings. *J. Mater. Chem. A* **3**, 12580–12602 (2015).
- G. H. Lee *et al.*, Highly stable, dual-gated MoS₂ transistors encapsulated by hexagonal boron nitride with gate-controllable contact, resistance, and threshold voltage. *ACS Nano* **9**, 7019–7026 (2015).
- H. Y. Chang *et al.*, High-performance, highly bendable MoS₂ transistors with high-k dielectrics for flexible low-power systems. *ACS Nano* **7**, 5446–5452 (2013).
- S. S. Sabri *et al.*, Graphene field effect transistors with parylene gate dielectric. *Appl. Phys. Lett.* **95**, 9–12 (2009).
- B. Chamlagain *et al.*, Mobility improvement and temperature dependence in MoSe₂ field-effect transistors on parylene-C substrate. *ACS Nano* **8**, 5079–5088 (2014). Correction in: *ACS Nano* **8**, 8710 (2014).
- Y. Zhao, Q. Zhou, Q. Li, X. Yao, J. Wang, Passivation of black phosphorus via self-assembled organic monolayers by van der Waals epitaxy. *Adv. Mater.* **29**, (2017).
- C. Mackin *et al.*, Chemiresistive graphene sensors for ammonia detection. *ACS Appl. Mater. Interfaces* **10**, 16169–16176 (2018).
- D. H. Kang *et al.*, Controllable nondegenerate p-type doping of tungsten diselenide by octadecyltrichlorosilane. *ACS Nano* **9**, 1099–1107 (2015).
- Z. He *et al.*, Revealing defect-state photoluminescence in monolayer WS₂ by cryogenic laser processing. *ACS Nano* **10**, 5847–5855 (2016).
- G. Lamour *et al.*, Contact angle measurements using a simplified experimental setup. *J. Chem. Edu.* **87**, 1403–1407 (2010).
- D. L. Williams *et al.*, Computerised measurement of contact angles. *Galvanotechnik* **101**, 2502–2512 (2010).
- M. T. Edmonds *et al.*, Creating a stable oxide at the surface of black phosphorus. *ACS Appl. Mater. Interfaces* **7**, 14557–14562 (2015).
- G. Kresse, J. Furthmüller, Efficient iterative schemes for ab initio total-energy calculations using a plane-wave basis set. *Phys. Rev. B Condens. Matter* **54**, 11169–11186 (1996).
- J. P. Perdew, K. Burke, M. Ernzerhof, Generalized gradient approximation made simple. *Phys. Rev. Lett.* **77**, 3865–3868 (1996).
- G. Kresse, From ultrasoft pseudopotentials to the projector augmented-wave method. *Phys. Rev. B* **59**, 1758–1775 (1999).
- S. Grimme, J. Antony, S. Ehrlich, H. Krieg, A consistent and accurate ab initio parametrization of density functional dispersion correction (DFT-D) for the 94 elements H–Pu. *J. Chem. Phys.* **132**, 154104 (2010).
- J. D. Pack, H. J. Monkhorst, “Special points for Brillouin-zone integrations”—a reply. *Phys Rev B* **16**, 1748–1749 (1977).
- W. Tang, E. Sanville, G. Henkelman, A grid-based Bader analysis algorithm without lattice bias. *J. Phys. Condens. Matter* **21**, 084204 (2009).
- M. Yu, D. R. Trinkle, Accurate and efficient algorithm for Bader charge integration. *J. Chem. Phys.* **134**, 064111 (2011).
- T. Low, M. Engel, M. Steiner, P. Avouris, Origin of photoresponse in black phosphorus phototransistors. *Phys. Rev. B* **90**, 1–5 (2014).
- H. Yuan *et al.*, Polarization-sensitive broadband photodetector using a black phosphorus vertical p-n junction. *Nat. Nanotechnol.* **10**, 707–713 (2015).
- J. M. Bastidas, J. L. Polo, E. Cano, Substitutional inhibition mechanism of mild steel hydrochloric acid corrosion by hexylamine and dodecylamine. *J. Appl. Electrochem.* **30**, 1173–1177 (2000).
- B. Long *et al.*, Non-covalent functionalization of graphene using self-assembly of alkane-amines. *Adv. Funct. Mater.* **22**, 717–725 (2012).
- X. Ling, H. Wang, S. Huang, F. Xia, M. S. Dresselhaus, The renaissance of black phosphorus. *Proc. Natl. Acad. Sci. U.S.A.* **112**, 4523–4530 (2015).
- J. M. Bastidas, J. D. E. Damborenea, A. J. Va, Butyl substituents in *n*-butylamine and their influence on mild steel corrosion inhibition in hydrochloric acid. *J. Appl. Electrochem.* **27**, 345–349 (1997).
- S. L. Yau, T. P. Moffat, A. J. Bard, Z. Zhang, M. M. Lerner, STM of the (010) surface of orthorhombic phosphorus. *Chem. Phys. Lett.* **198**, 383–388 (1992).

Waterproof molecular monolayers stabilize 2D materials

Table of contents

1. Coating methods and protection testing

- I. Coating of *n*-hexylamine (C₆H₁₃NH₂) onto unstable 2D flakes of black phosphorous (BP), MoTe₂, WTe₂, WSe₂, TaS₂, and NbSe₂
- II. Coating of *n*-hexylamine onto relatively stable WS₂
- III. Coating other alkylamines and control molecules onto BP
- IV. Protection testing results for alkylamines coated BP

2. Characterization methods

- I. Contact angle measurement
- II. Optical microscopy and Raman
- III. X-ray photoelectron spectroscopy (XPS) and surface coverage estimation
- IV. Atomic force microscopy (AFM)

3. First-principles calculation

- I. Calculation method details
- II. Adsorption energies of different configurations
- III. Surface coverage for hexylamine–BP system
- IV. Energy barrier calculations during kinetic transport for hexylamine–BP system

4. Photodetector device

- I. BP photodetector fabrication
- II. Channel BP characterization with AFM
- III. Measurement setup for characterizing BP photodetectors
- IV. Photothermoelectric photocurrent generation in BP photodetectors

5. Removability testing

- I. *n*-octylamine/BP
- II. *n*-hexylamine/TMDs

6. Protection techniques comparison

1. Coating methods and protection testing

I. Coating of n -hexylamine ($C_6H_{13}NH_2$) onto unstable 2D flakes of black phosphorous (BP), $MoTe_2$, WTe_2 , WSe_2 , TaS_2 , and $NbSe_2$

In our experiment, n -alkylamine (Sigma-Aldrich, 99%) was used as purchased. The two dimensional (2D) crystals are mechanically exfoliated and transferred or directly chemical vapor deposition (CVD) onto a piece of silicon wafer (with a 190 nm SiO_2 surface layer), denoted as 2D/ SiO_2 /Si, after SiO_2 /Si substrates were washed in water, isopropyl alcohol (IPA) and acetone, respectively, by sonication for 10 mins, followed by the annealing in air for 30 min at 200 °C to remove the absorbed water on surface. The exfoliation was done with Scotch Tape in a glove box for BP, but in the air for other four 2D materials: $MoTe_2$, WTe_2 , WSe_2 , TaS_2 , and $NbSe_2$. In the following, coating of n -hexylamine onto BP is taken as the example to introduce the whole coating procedure.

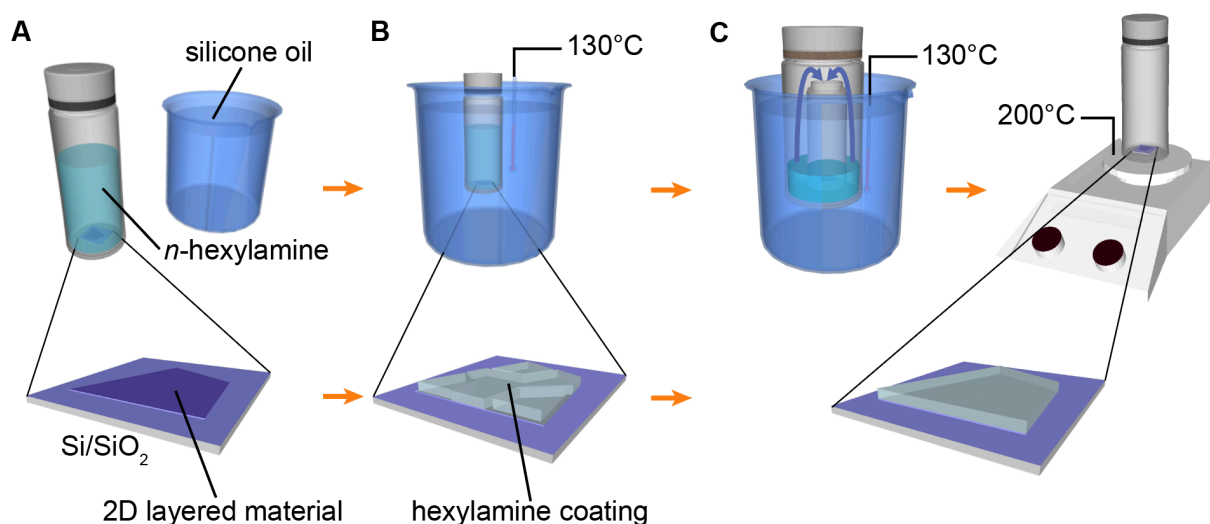


Fig. S1. **A**, The layered materials on SiO_2 /Si wafer are immersed in the liquid n -hexylamine contained in a glass vial, which is then capped and placed inside the silicone oil. **B**, In the first step, the oil bath is heated up to 130 °C and maintained for 20 minutes. Hexylamine is coated on the layered material with minor defects. **C**, In the second step, the sample is steamed in the amine vapor under 130 °C for 20 min, followed by an annealing in 200 °C for 30 min. This step is aimed for fixing the defects in n -hexylamine overlayer.

The whole coating process can be divided into two steps, which is performed in the Acrylic glove box, as schematically explained in the Fig. S1. Such glove box can maintain a certain level (~ 30 ppm) O_2 and H_2O , which is necessary for uniform oxidation and hydroxylation of BP surface layer during amine growth. In brief, $2D/SiO_2/Si$ samples were completely immersed in excess amount (2 - 10 mL, depending on the size of reactor vial or petri dish) of *n*-hexylamine contained in a glass vial or petri dish, covered with a cap. Such vial or petri-dish based reactor was immersed into a silicone oil bath or sitting on a hotplate which will be heated up for the first step growth. This step growth was maintained about 20 min at 130 °C and then cooled down to room temperature (RT) and kept for half an hour to complete the first step growth. After this, samples were taken out and rinsed with hexane to remove the attached amine residues. For the second step growth, the samples under heating at 130°C will be steamed in the amine vapor for about 20 min, with the subsequent cooling down to RT for another half an hour. After gently rinsed with hexane and dried, the samples were transferred to another glove box with low O_2 and H_2O levels (< 0.1 ppm) to be sealed in a glass vial for the final simple post-growth annealing at 200 °C for 30 min. After cooling down, the sample was then ready for characterization and testing.

n-hexylamine coating parameters were optimized step by step based on BP (Table S1). The similar parameters are applied for *n*-hexylamine coating onto other 2D materials (Table 1 in main text), and the parameters are optimized for other amine molecules with different carbon chain lengths onto BP (Table S2 and S3).

II. Coating of *n*-hexylamine onto relatively stable WS_2

The coating protocols are slightly different from above. As-purchased *n*-hexylamine was directly used for the coating without further purification. WS_2 samples were grown onto SiO_2 (300 nm)/Si substrates by CVD method.^[1] Subsequent deposition of *n*-hexylamine was realized by one-step growth. In order to drive oxygen out of *n*-hexylamine before the growth, *n*-hexylamine was boiled at ~ 130 °C for 30 min in air. Then, the $WS_2/SiO_2/Si$ samples were immediately immersed into boiling *n*-hexylamine carefully and covered with the cap (note: the cap should not be fully tightened to avoid high pressure building-up in the bottle that can lead to explosion). After growth and subsequent cooling down to room temperature, the samples were collected and gently rinsed with hexane followed by immediate drying with N_2 gas blowing. Similarly, as the two-step growth

for other 2D material, a simple post-growth annealing was also applied for amine coated WS₂/SiO₂/Si at 200 °C for 30 min in the argon and then the samples are ready for testing and characterization.

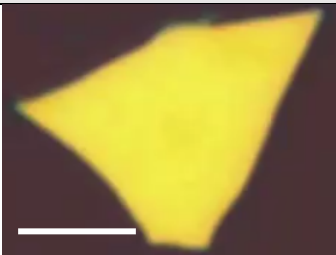
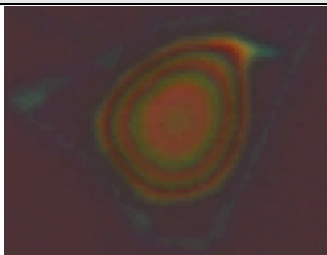
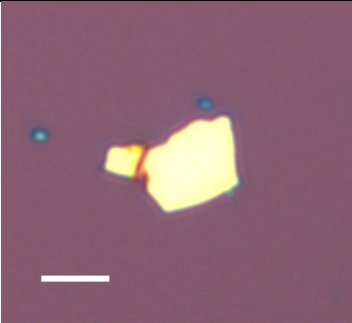
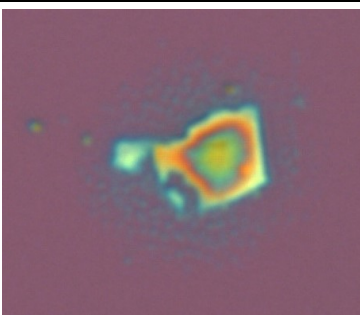
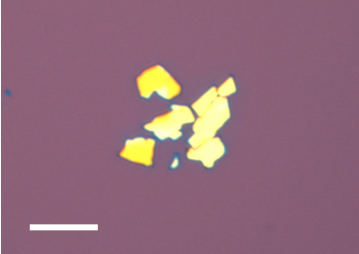
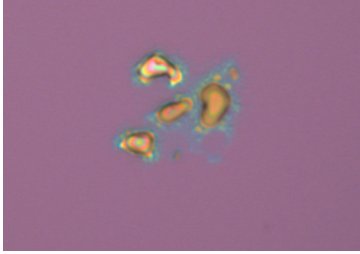
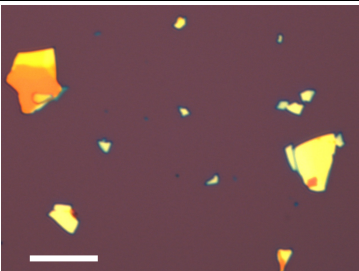
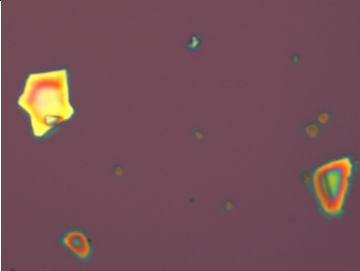
III. Coating other alkylamines and control molecules onto BP

Besides *n*-hexylamine (*n*-C₆H₁₃NH₂), BP crystals were also coated with other linear alkylamines with different carbon chain lengths, including *n*-butylamine (*n*-C₄H₉NH₂), *n*-pentylamine (*n*-C₅H₁₁NH₂), *n*-octylamine (*n*-C₈H₁₇NH₂), *n*-decylamine (*n*-C₁₀H₂₁NH₂), *n*-undecylamine (*n*-C₁₁H₂₃NH₂). The main difference in coating process for these amine molecules lies in the coating temperatures, which are normally set to be below or close to the boiling point of each amine molecule for safety considerations. The coating parameters are summarized in the table S2 below. After the coating, all these amine-coated BP samples were tested using H₂O₂ as etchant, where the protection effect is evaluated by comparing the optical microscope images before and after the H₂O₂ etching (table S3).

Furthermore, two control experiments were performed in terms of the molecule types used for coating. First, we tested benzylamine (C₆H₅CH₂NH₂), which is a non-linear alkylamine. Non-linear benzylamine is expected to be challenging to form a high-coverage dense monolayer on the surface of 2D material as there exists un-coverable gap between the benzene ring structures, thus affecting the protection as demonstrated below. Second, amino-group-free alkane molecule, i.e. *n*-hexane (*n*-C₆H₁₄), was tested on BP. As presented in table S3, *n*-hexane coating does not have any protection capability. This further consolidates our proposed monolayer link model between alkylamine and BP as discussed detailed in the main text.

IV. Protection testing results for alkylamines coated BP

Table S1. Optimization of coating parameters of *n*-hexylamine on BP. The etching method with H₂O₂ (30% wt. in H₂O) etchant/oxidant is as follows: dip BP into H₂O₂ for 20 sec, remove BP from H₂O₂, and leave dipped BP for 2 mins in air. Scale bars are 20 μm.

	Before applying oxidant	After applying oxidant
<p>Pure fresh BP (<u>not protected</u>)</p>		
<p><i>n</i>-hexylamine-BP: Immersed in <i>n</i>-hexylamine for 6 days at RT (<u>not protected</u>)</p>		
<p><i>n</i>-hexylamine-BP: 70 °C & 20 mins (<u>not protected</u>)</p>		
<p><i>n</i>-hexylamine-BP: 90 °C & 20 mins (<u>not protected</u>)</p>		

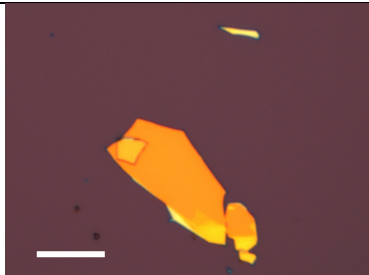
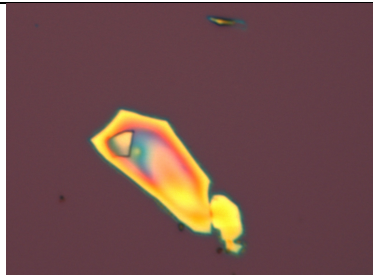
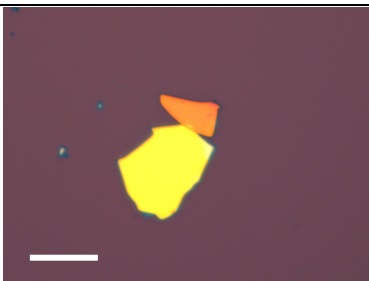
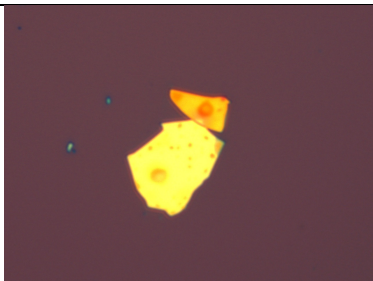
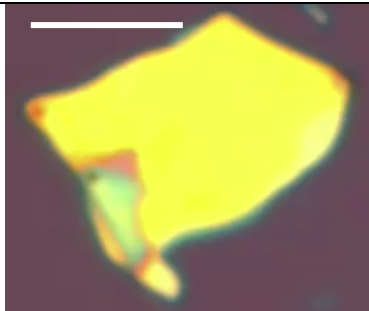
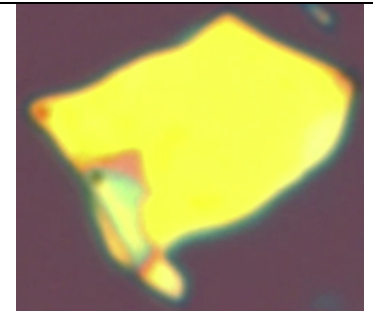
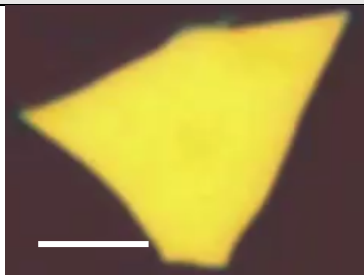
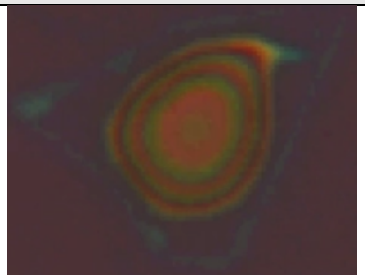
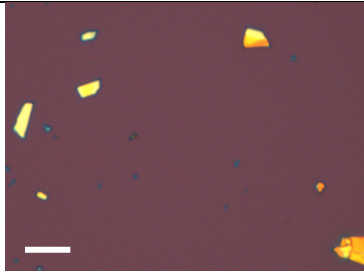
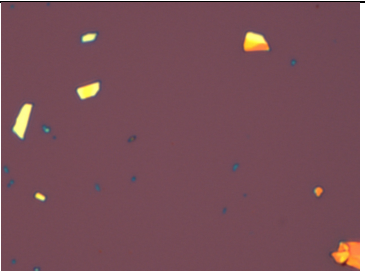
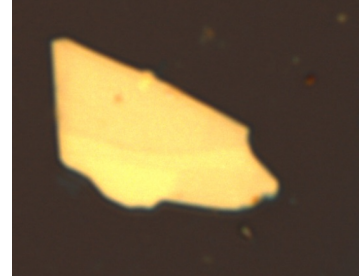
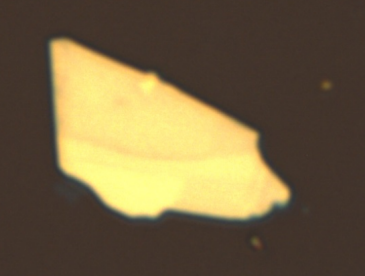
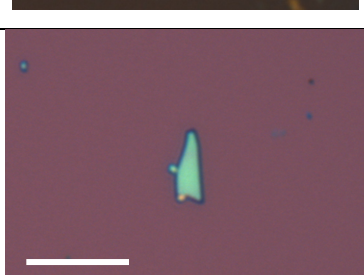

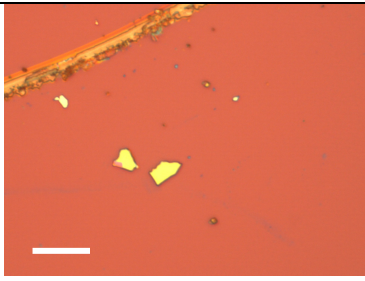
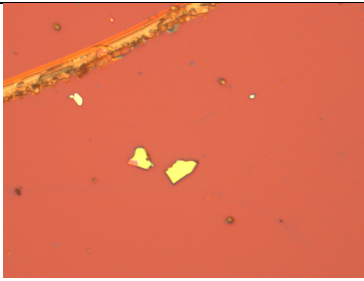
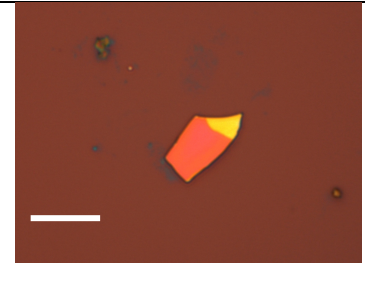
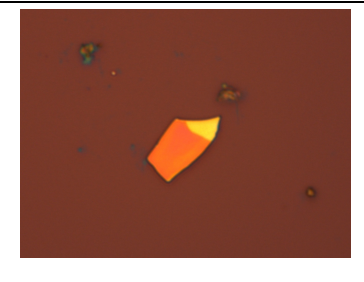
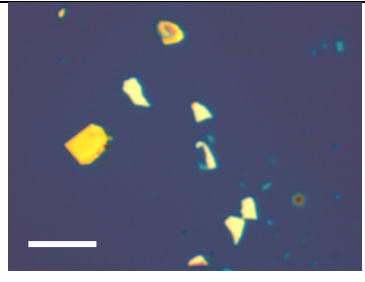
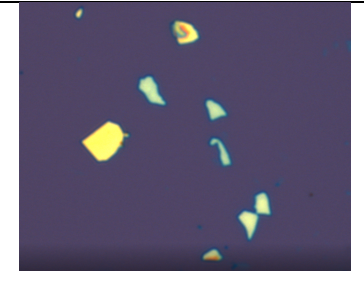
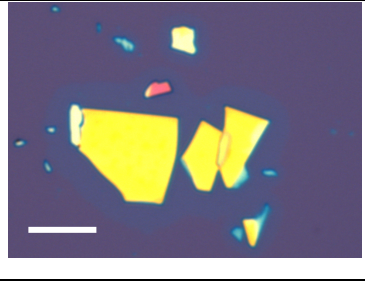
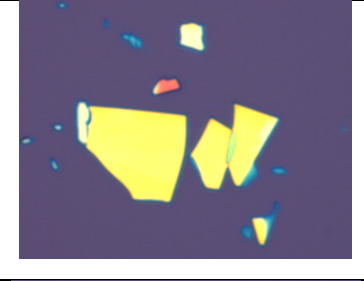
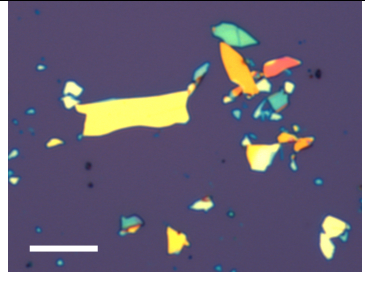
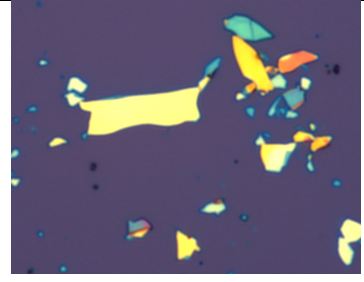
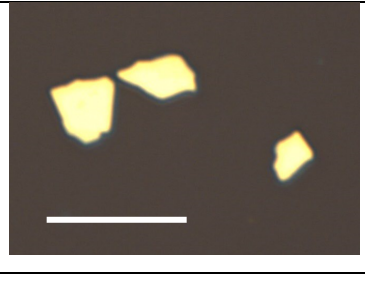
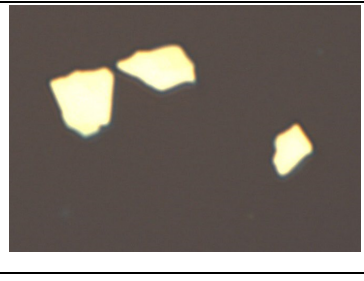
<p><i>n</i>-hexylamine-BP: 110 °C & 20 mins <u>(not protected)</u></p>		
<p><i>n</i>-hexylamine-BP: 130 °C & 20 mins <u>(partially protected)</u></p>		
<p><i>n</i>-hexylamine-BP: two-step coating aforementioned <u>(protected)</u></p>		

Table S2. Protection testing for different alkylamines and hexane. The optical microscope images were taken before and after etching/oxidation of BP flakes with the same etching method as described above.

	Coating temperature (°C)	Before applying oxidant	After applying oxidant
Pure fresh BP (<u>not protected</u> , the same as Table S1)	No treatment		
<i>n</i> -butylamine-BP	90		
<i>n</i> -pentylamine-BP	110		
<i>n</i> -hexylamine-BP	130		

<i>n</i> -octylamine-BP	140		
	160		
<i>n</i> -decylamine-BP	120 (partially protected)		
	150		
	180		
<i>n</i> -undecylamine	180		

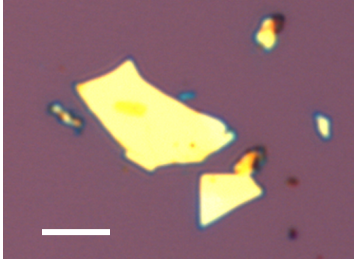
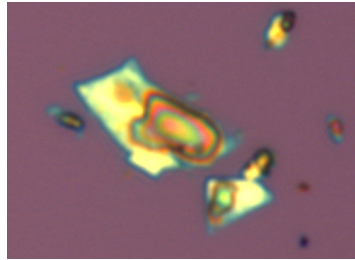
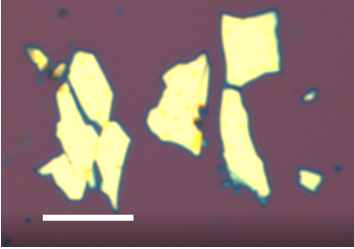
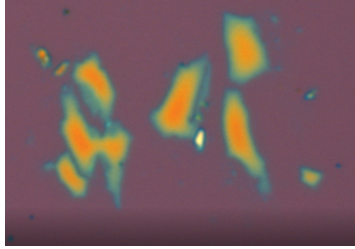
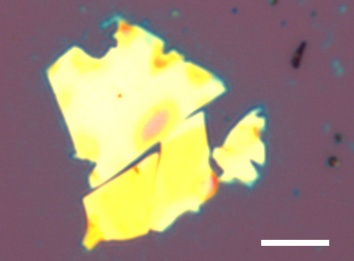
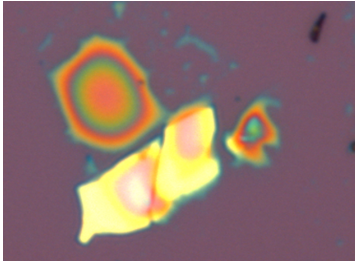
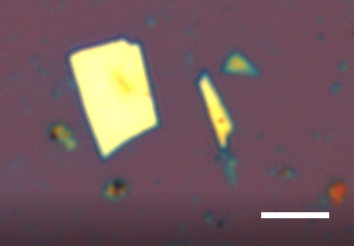
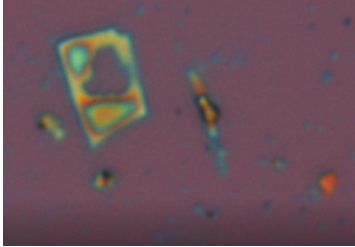
<p>hexane-BP <u>(not protected)</u></p>	<p>90</p>		
<p>benzylamine-BP <u>(not protected)</u></p>	<p>120</p>		
	<p>150</p>		
	<p>180</p>		

Table S3. Coating parameters used for coating amines and hexane on 2D materials.

	Boiling point (°C)	Coating temperature (°C)	Coating time	Post-coating annealing
<i>n</i> -C ₄ H ₉ NH ₂	~ 78	90	Two steps (1 st step: 20 min heated in liquid; 2 nd step: 20 min steamed in vapor)	200 °C for 30 min in argon
<i>n</i> -C ₅ H ₁₁ NH ₂	105	110		
<i>n</i> -C ₆ H ₁₃ NH ₂	131.5	130		
<i>n</i> -C ₈ H ₁₇ NH ₂	~176	140-160		
<i>n</i> -C ₁₀ H ₂₁ NH ₂	~217	150-180		
<i>n</i> -C ₁₁ H ₂₃ NH ₂	~240	180		
C ₆ H ₅ CH ₂ NH ₂	185	180 (not protected)		
<i>n</i> -C ₆ H ₁₄	68.7	80 (not protected)		

2. Characterization methods

I. Contact angle measurement

The contact angle measurement was done using a home-made zoom-in microscope.^[2,3] The analysis is processed with the “contact angle” plug-in software developed by Marco Brugnara in ImageJ software. The measurement results on SiO₂ (figs. S2A and B) indicate no *n*-hexylamine was deposited onto SiO₂/Si wafer. This test also verifies the eligibility of AFM measurement on height change of 2D flakes before and after amine coating, as the flake thickness can be consistently referenced to the surface of SiO₂/Si wafer.

On the contrary, for WS₂ (figs. S2C and D) and BP (figs. S2E and F), there is an increase in the contact angle after coating of *n*-hexylamine, indicating the successful coating of amine molecules on WS₂ and BP. It should be noted that the contact angle only qualitatively reveals the surface wettability for these two materials, as the surface of Si wafer is not totally covered by WS₂ or BP flakes.

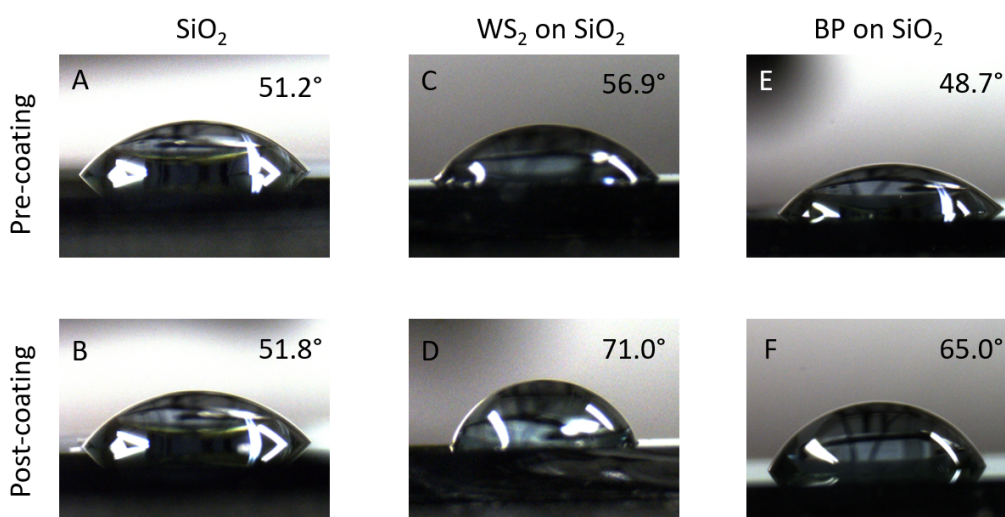


Fig. S2. Contact angles of water droplet on different substances. The images of a water droplet on (A, B) SiO₂, (C, D) WS₂ flakes on SiO₂, and (E, F) BP flakes on SiO₂ before and after *n*-hexylamine-coating process, respectively. The contact angles are marked within the images. Note that since the flakes are scattered on wafer and cover about 10% of the surface area, the angle in these image is a qualitative revelation of the hydrophobicity of the *n*-hexylamine-coated layer. The angles are averaged from ten sites on each sample.

II. Optical microscopy and Raman spectroscopy

All the 2D samples in this work were imaged using an optical microscope (Axio Imager (Carl Zeiss)). The Raman spectra of all the 2D materials were measured using a Horiba Jobin-Yvon HR800 Raman Spectrometer. The laser spot size is 1 μm in diameter and a 100 \times objective with an NA of 0.90 was used. The 532 nm frequency-doubled Nd:YAG excitation laser was used with the laser power on the sample set about 1 mW. 1800 lines/mm grating was used for Raman measurement. All the Raman spectra are original data with only background subtraction, and we performed the measurement under the same alignment/orientation each time.

III. X-ray photoelectron spectroscopy (XPS) and surface coverage estimation

The surface chemical analysis was carried out via a Thermo Scientific K-Alpha X-ray XPS using a monochromated Al-K α X-ray source ($h\nu = 1486.6$ eV). Each data point in the time-evolved oxidation measurement was done by opening the pump lid and letting the sample be exposed to ambient air for a certain amount of time, and then re-pumping the chamber and doing the measurement. XPS spectra of a HA-BP as coated, after 2 days, and after 46 days are shown in Fig. 2F, and the spectrum is deconvoluted by two P 2p main peaks (centered at 129.68 eV and 130.68 eV), and three oxidized phosphorous peaks (centered at 131.48 eV, 132.46 eV, and 134.08 eV).^[4] The phosphorous percentage is calculated by analyzing the composition of these peaks, and fitted by an exponential growth curve in Fig. 2G. The curve has the form $\eta = A - B(1 - e^{-\frac{t}{\tau}})$, where η is the percentage of oxidized phosphorous, A and B are fitting parameters, and τ is the time constant. According to the fitting curves of BP and HA-BP in Fig. 2G, we find that $\tau_{HA-BP} \sim 32\tau_{BP}$. From the diagram, the whole curve of HA-BP clearly cannot be fitted by a single exponential function. A second curve starting at the ~ 100 hours with a much larger time constant is shown, and this could be ascribed to the saturation of the passivation layer, where the passivation layer itself could drastically slow down the further oxidation process. However, it is seen that after 48 hours, the oxidation of HA-BP clearly slows down, which is fitted by the dashed curve. This slow-down may be due to the saturation of surface oxidation of phosphorous and the phosphorous oxide forms a passivation layer that further protects the phosphorous beneath. According the fitting curves of BP and HA-BP, we find that $\tau_{HA-BP} \sim 32\tau_{BP} (< 50h)$ at the starting period and $\tau_{HA-BP} \sim 238\tau_{BP} (>$

50h). The change of tunneling rate of oxygen should follow an Arrhenius relation as $\exp(-\Delta E/k_B T) < 1/32$, thus $\Delta E > 0.09$ eV, which indicates that the coverage should be above 66.7% (whose tunneling barrier is 0 eV for O₂) by combining the calculated results in the work.

IV. Atomic force microscopy (AFM)

For BP measurement, tapping mode atomic force microscopy is done using a Nanosurf Flex-Axiom AFM enclosed in a glove box with an inert environment containing <0.1 ppm O₂ and <0.1 ppm H₂O to avoid corrosion. For WSe₂ measurement, the measurements were performed on Dimensional Icon system (Bruker, USA) in tapping mode with ultrasharp probes (OMCL-AC160TS, Olympus, Japan). The resonance frequency and spring constant for the probes are about 285 kHz and 26N/m, respectively. The thickness and roughness were obtained by analyzing the AFM height image with Scanning Probe Image Processor software (Image Metrology Aps, Denmark).

3. First-principles calculation

I. Calculation method details

Calculations are performed using Vienna ab initio simulation package (VASP)^[5] with the generalized gradient approximation of Perdew-Burke-Ernzerhof (PBE)^[6] for the exchange-correlation potential and a projector augmented wave (PAW) method.^[7] The DFT-D3 method^[8] was adopted to account for the van der Waals interactions. Supercells containing a vacuum spacing larger than 15 Å were used to model the BP and WS₂ surfaces. The kinetic energy cutoff for plane wave functions is set to 500 eV and the energy convergence threshold is set as 10⁻⁴ eV. The Monkhorst-Pack k-mesh^[9] of 5×5×1 is employed to sample the irreducible Brillouin zone. The atoms were fully optimized and the maximum force on each atom is less than 0.01 eV/Å. Bader's charge analysis is done for analyzing the charge distribution after proton transfer.^[10,11] For hexylamine-BP system, two BP bilayers were used for the model with the bottom bilayer was fixed during optimization (not shown in following figures); while for hexylamine-WS₂ system, only a single layer of WS₂ was included in the model.

II. Adsorption energies of different configurations

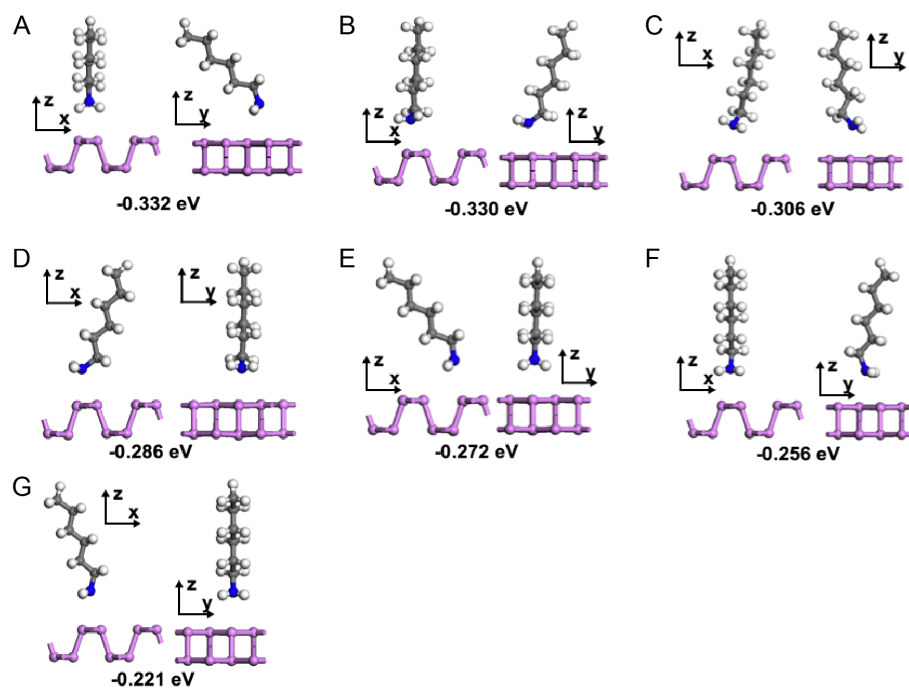


Fig. S3. Seven different configurations for direct adsorption of *n*-hexylamine on BP. For each configuration, the front view and side view are shown, and the adsorption energy is marked under each configuration. The largest adsorption energy is only 0.33 eV.

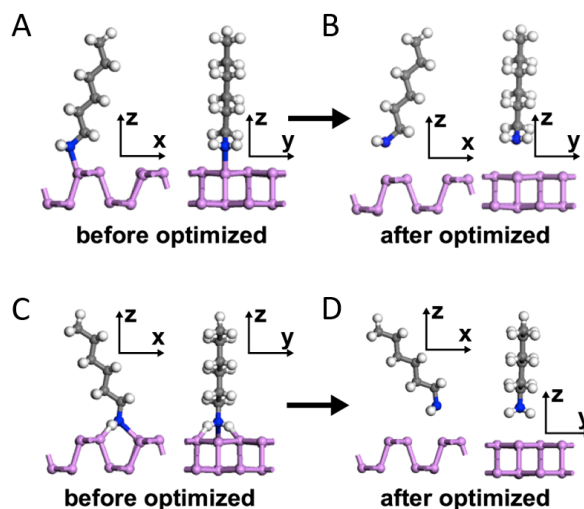


Fig. S4. (A and C) For direct adsorption of *n*-hexylamine on BP, two special initial configurations have been tested, in which *n*-hexylamines are chemically bonded with BP. (B and D) After optimization, *n*-hexylamines in these two configurations have been repelled by BP, indicating that direct chemical bonding between *n*-hexylamines and BP is not possible.

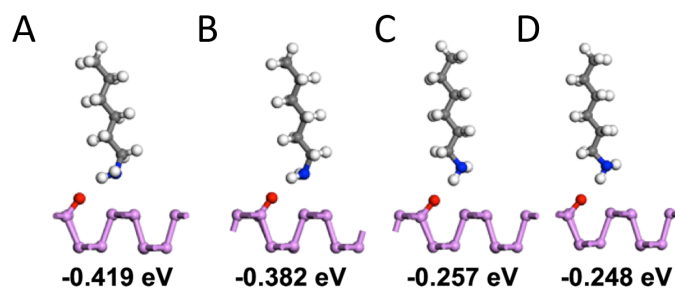


Fig. S5. Four different configurations for adsorption of *n*-hexylamine on oxidized BP. The largest adsorption energy is 0.419 eV, indicating that oxidization of BP can enhance adsorption between BP and *n*-hexylamine.

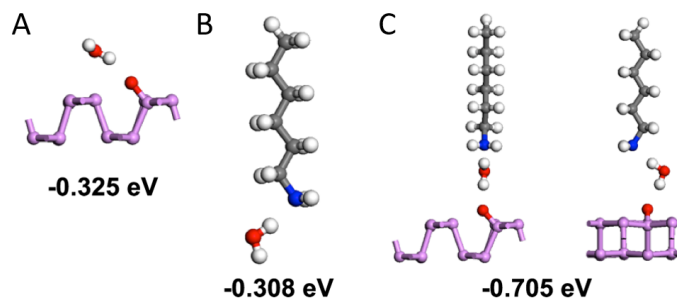


Fig. S6. (A) The lowest energy configuration for adsorption of H₂O on oxidized BP. (B) The lowest energy configuration for adsorption between *n*-hexylamine and H₂O. (C) The lowest energy configuration for H₂O-mediated adsorption, where the adsorption energy consists of the two binding energies between H₂O molecule and oxidized BP and between H₂O and *n*-hexylamine.

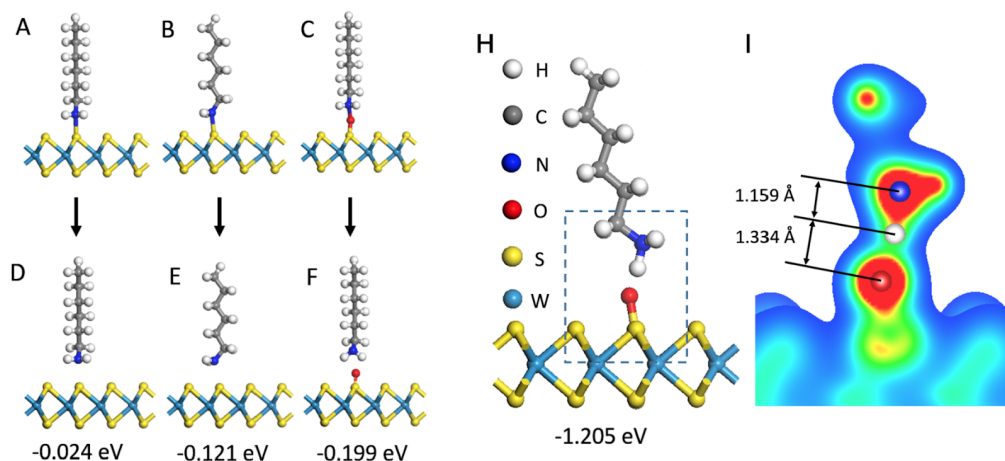


Fig. S7. For the vertical adsorption configurations of *n*-hexylamines on WS₂/oxidized WS₂, three different initial configurations are tested: (A, B) *n*-hexylamine connected with S atom with two orientations, and (C) *n*-hexylamine connecting to oxidized WS₂. From all of these configurations, WS₂/oxidized WS₂ repel *n*-hexylamines and the chemical bonds are broken (D-F), revealing that direct chemical bonding between *n*-hexylamines and WS₂/oxidized WS₂ is not possible. The adsorption energies are 0.024, 0.121 eV and 0.199 eV, respectively. (H) The most stable configuration with *n*-hexylammonium connected with the oxidized WS₂ sample, which has an adsorption energy of 1.205 eV. (I) The contour map of valence electron density on the common plane of N, O, H, and C.

III. Surface coverage for hexylamine-BP system

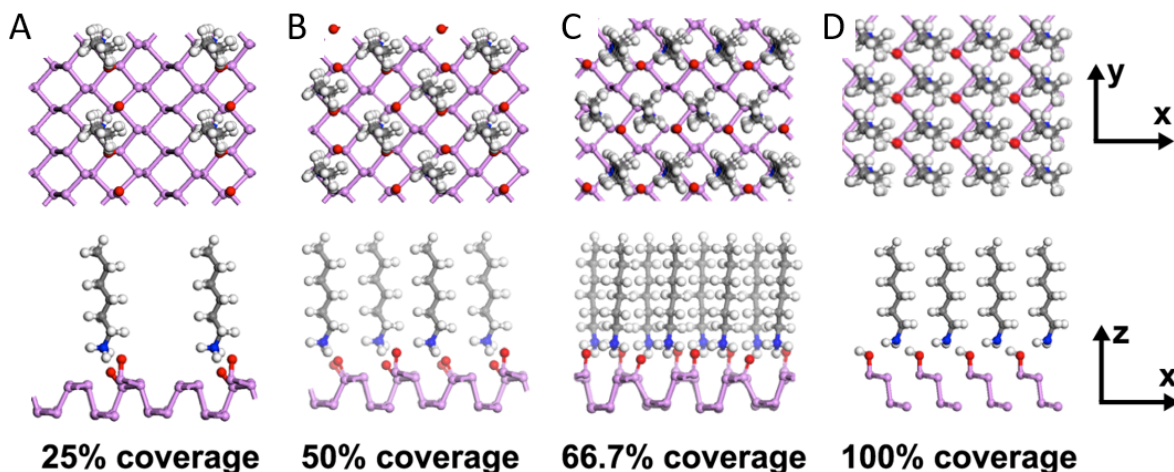


Fig. S8. The models of (A) 25% coverage (binding energy 1.07 eV/*n*-hexylamine), (B) 50% coverage (binding energy 1.2 eV/*n*-hexylamine), (C) 66.7% coverage (binding energy 1.18 eV/*n*-

hexylamine), and **(D)** 100% coverage (binding energy 0.58 eV/*n*-hexylamine), used for calculating the penetration energy barrier of H₂O molecules and O₂ molecules. Note that in 100% coverage, the footprint of *n*-hexylamine molecules completely covers the BP, so that no denser coverage could be further achieved. The first row are top views and the bottom row are side views of corresponding configurations.

IV. Energy barrier calculations during kinetic transport for hexylamine–BP system

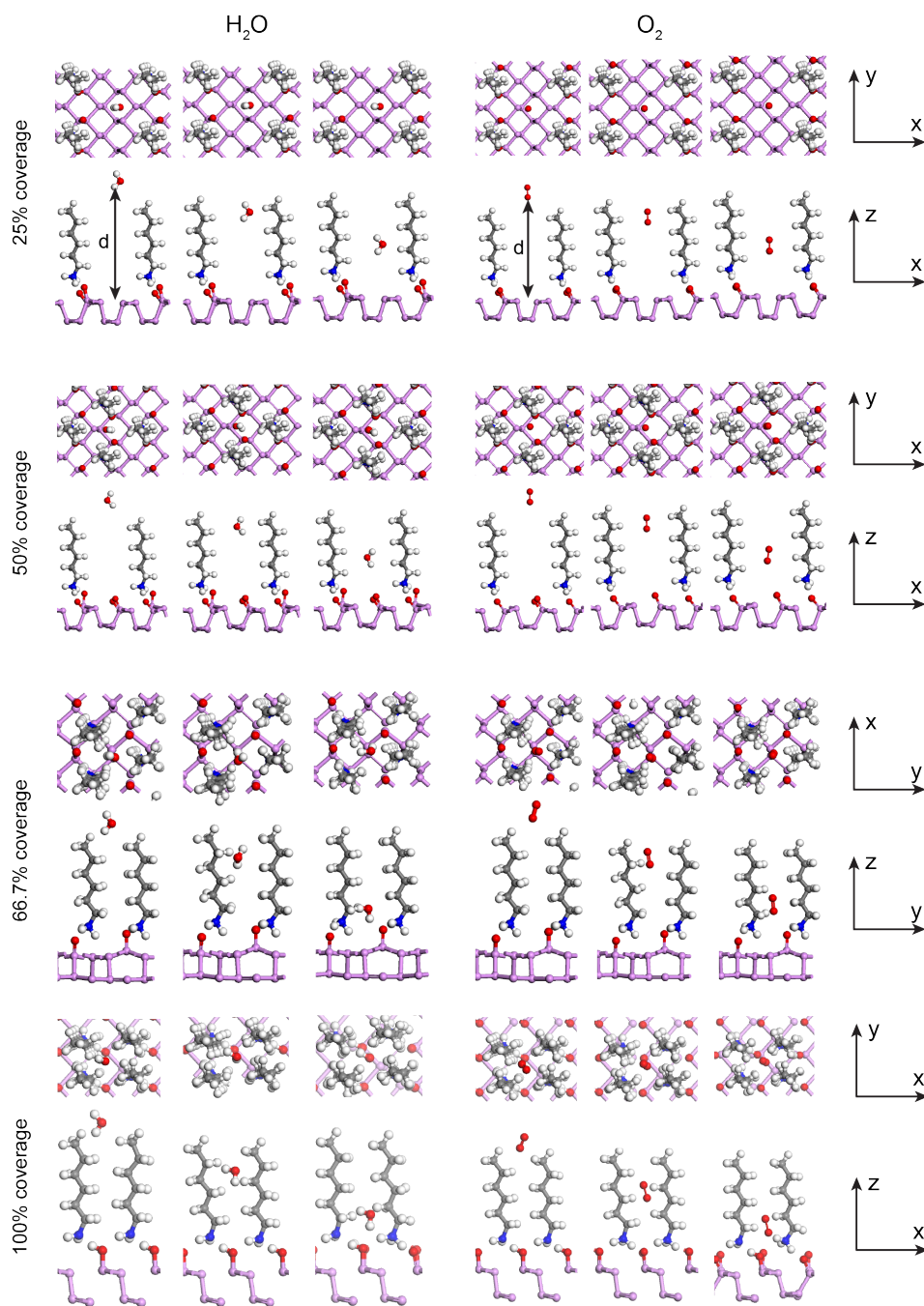


Fig. S9. The structures of HA-BP used for calculating H₂O and O₂ molecules penetrating through the *n*-hexylamine coating. For each coverage and penetrating molecule type, three different locations are shown (far, middle, and close to the BP surface respectively), and each location is shown in two perspectives which are top view and side view. The distance d is defined in the first two figures of H₂O and O₂ in 25% coverage.

4. Photodetector device

I. BP photodetector fabrication

First, the pattern with Ti(15 nm)/Au(150 nm) for marking was fabricated onto SiO₂(190 nm)/Si substrate by photolithography. These Ti/Au patterns help to locate the BP flakes that will be exfoliated onto the SiO₂/Si substrate subsequently. Before BP exfoliation, the SiO₂/Si substrate was annealed/dried in air for 30 minutes at > 200°C to remove humidity from air and then transferred into a glove box. Exfoliation of BP flakes onto SiO₂/Si was performed in the glove box. After exfoliation, the metallic electrode pads of Ti(15 nm)/Au(200 nm), fabricated onto BP flakes sitting on SiO₂/Si substrate were defined by electron-beam lithography (EBL) using PMMA as the resist mask, where the active channel width and length are kept comparable for both *n*-hexylamine-protected and the control BP detectors. After liftoff of PMMA, the BP photodetector fabrication was completed for the BP control sample. To prepare the *n*-hexylamine-protected BP detector, the amine molecules were coated onto BP devices with the aforementioned method prior to characterization.

II. Channel BP thickness measurement with AFM

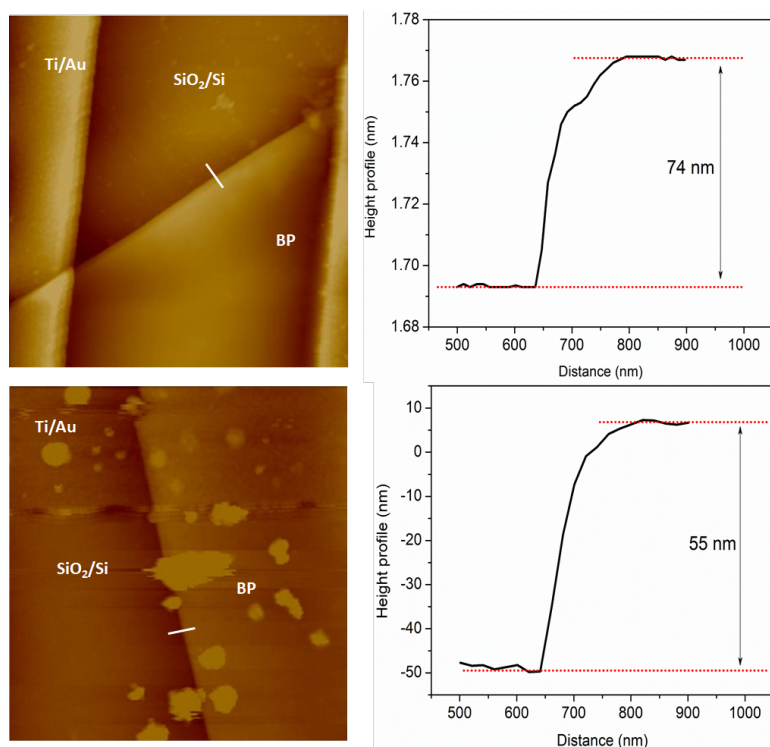


Fig. S10. Height profile for the channel of BP flakes in pure BP control device with a thickness of 74 nm (upper panel) and HA-BP device with a thickness of 55 nm (lower panel). The particles on the HA-BP device are residues from H₂O₂ solution after treatment of the device with H₂O₂ etchant. The dimension of the two AFM topographic images is 5 μm × 5 μm.

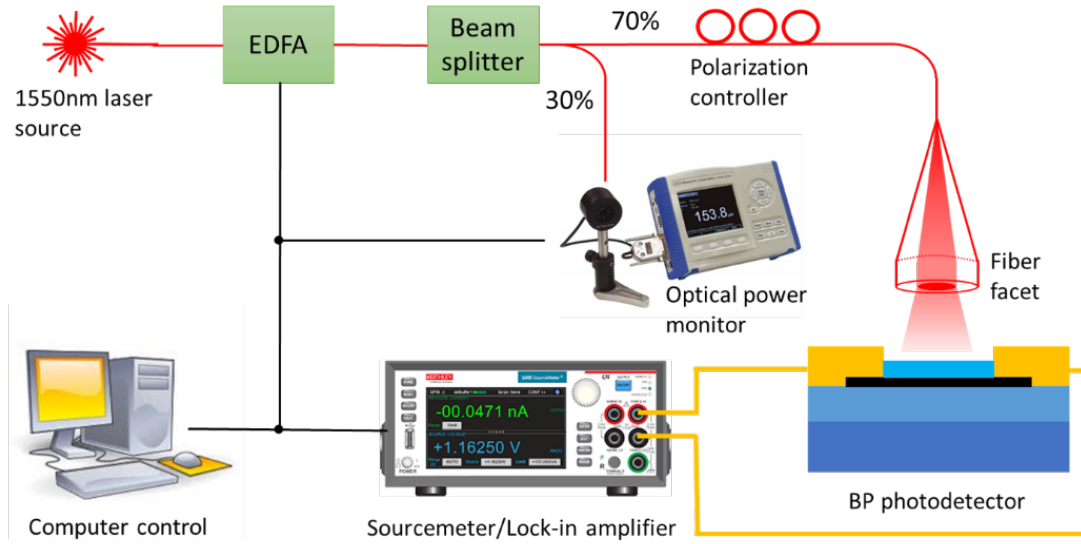


Fig. S11. Schematic of the photodetector measurement setup.

III. Measurement setup for characterizing black phosphorus photodetectors

Figure S11 shows a schematic diagram of the system setup. An all-fiber system was used to deliver probing light to the photodetector. Light from a 1550 nm tunable external cavity laser was coupled into an optical fiber and amplified by an Erbium Doped Fiber Amplifier (EDFA, Amonics). The EDFA output was split into two beams: 30% of the light was monitored by an optical power meter (Newport 1918A) to record the light intensity in real-time during the experiment. 70% of the light passed through a fiber with a cleaved facet and incident upon the black phosphorus photodetector at a fixed incident angle of 15 degrees. Due to the highly anisotropic optical and electrical properties of black phosphorus, an inline polarization controller was used to adjust the polarization of light to maximize the photocurrent. A source meter (Keithley SMU2450) was used to measure the photocurrent generated by the photodetector at zero bias while laser was working on continuous wave mode. To assess the photoresponsivity under bias condition, the laser light was modulated at 30 kHz and a trans-impedance amplifier (SRS SR570) was used to apply the bias. The amplified photocurrent was recorded using a lock-in amplifier (SRS SR844). We use finite-difference time-domain (FDTD) simulations to quantify the optical power absorbed by the photodetector, shown in Figure S12. The laser light from the fiber facet is modeled as a Gaussian beam with a beam waist of about 5.5 μm according to our simulations. A power monitor was used

to evaluate the power flux passing through the photodetector. The model indicates that 23% of light exiting from the fiber was captured within the active area of the photodetector. Detector responsivity was calculated by normalizing the measured photocurrent by the incident optical power on the photodetector.

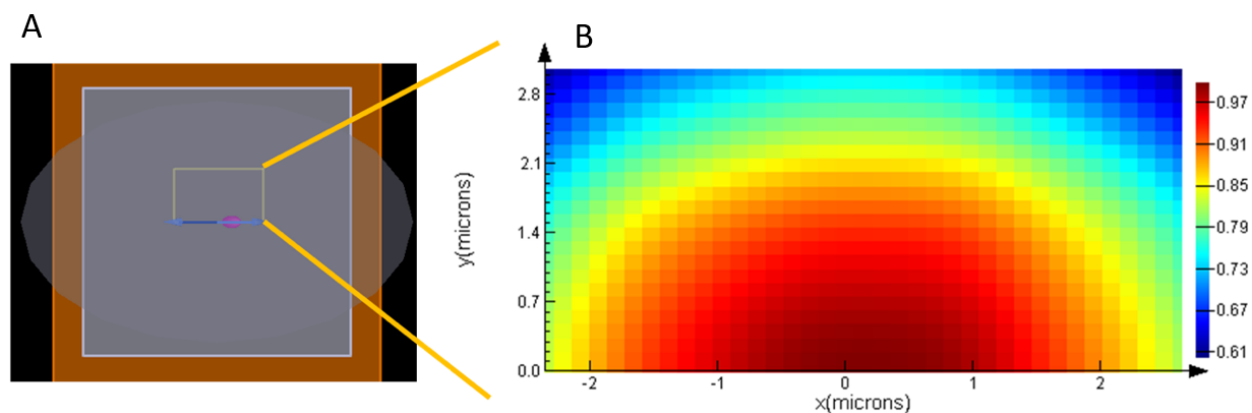


Fig. S12. (A) yellow rectangle showed the relative position between the active region of a 5 μm by 3 μm size photodetector and the center of incident laser light at optimized coupling condition. (B) electromagnetic field distribution on the photodetector.

IV. Photothermoelectric photocurrent generation in BP photodetectors

We experimentally investigated the photocurrent generation mechanism in the BP detectors by mapping the photocurrent as a function of the incident beam location. As shown in Figure S13A, the fiber light source, mounted on a linear translational motion stage, was traversed across the detector active area while the photocurrent was monitored. Figure S13B and 13C plot the measurement results obtained on black phosphorus detectors with and without inhibitor protection, respectively. In both types of devices, photocurrent reaches maximum when the illumination spot is close to the metal junctions and passes through zero close to the center of the device. This behavior is an unequivocal signature of photothermoelectric response.^[12,13]

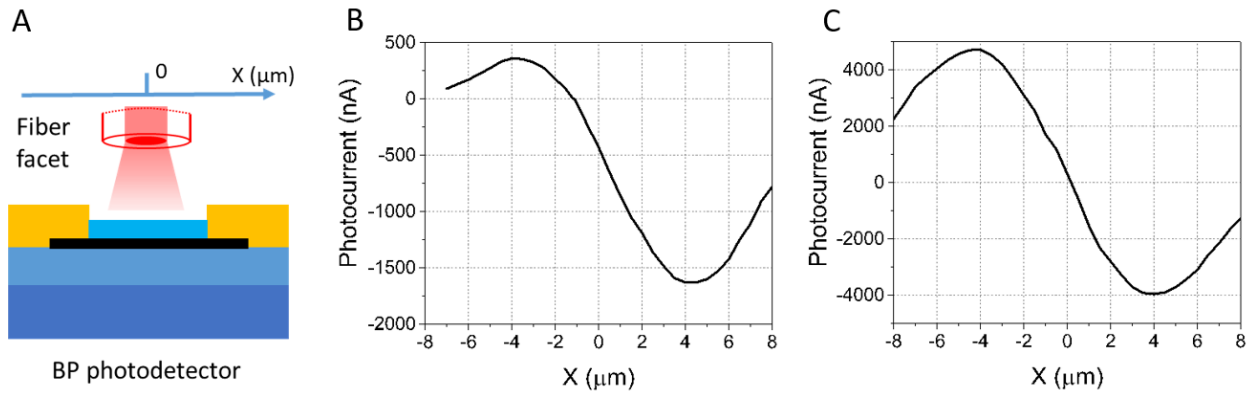


Fig. S13. (A) Illustration of photocurrent scanning set-up and photocurrent generation cross-section along the BP photodetector (B) with and (C) without *n*-hexylamine coating at zero bias condition.

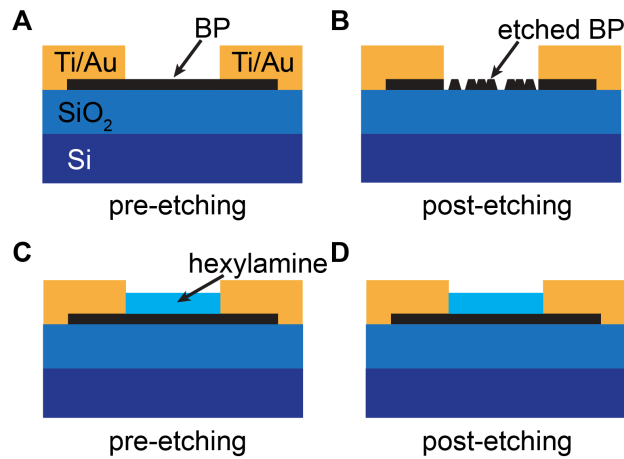


Fig. S14. A schematic diagram of the layout of the photodetector etching test. (A, B) The bare BP device before and after etching. (C, D) Before and after hexylamine coated device etching test.

5. Removability testing

I. *n*-alkylamine/BP

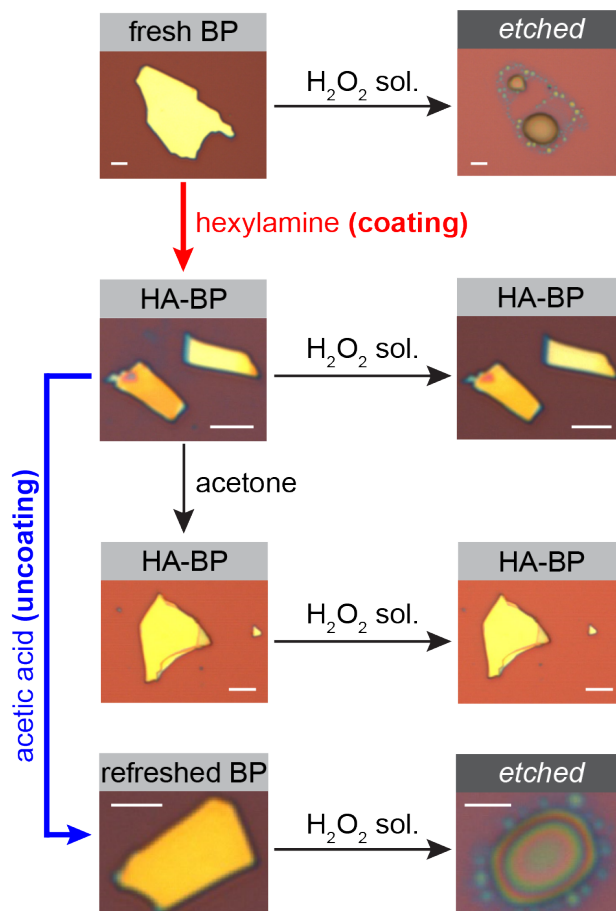


Fig. S15. Removability of *n*-hexylamine coating on BP by organic acid. First row, the fresh BP as a starting point, is etched by H₂O₂ solution (30 wt% in H₂O). After coating *n*-hexylamine on fresh BP, HA-BP is resistant to H₂O₂ etching, as shown in the second row. In the third row, the HA-BP sample is treated with acetone for 20 mins, but still resistant to H₂O₂ etching; while by applying glacial acetic acid or acetone/HCl (acetone : HCl (37 wt% in H₂O) = 1:1 in volume ratio) solution on the HA-BP for 20 mins at room temperature, the *n*-hexylamine coating is removed, and the BP can be again etched by H₂O₂ solution, as shown in the last row. Red arrow indicates the coating process, and blue arrow the uncoating process. The scale bars are 10 μm.

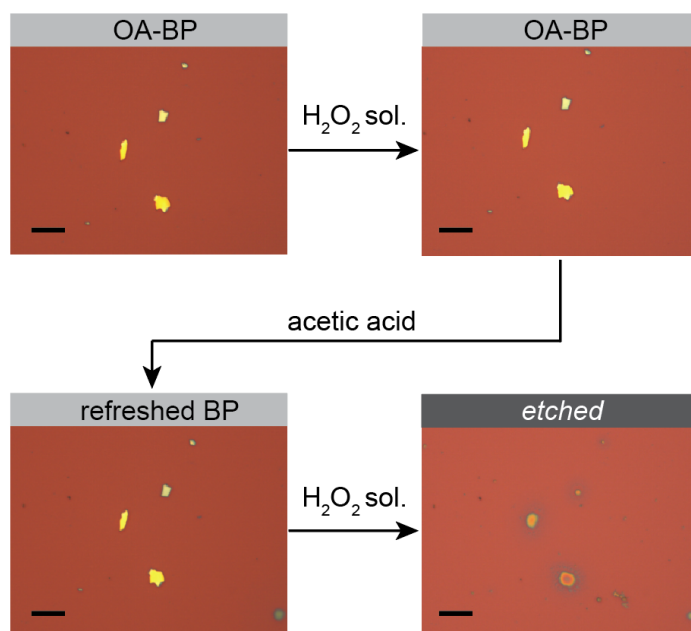


Fig. S16. Removable *n*-octylamine coating on BP. First row, the BP has been coated with octylamine and dipping inside hydrogen peroxide without etching demonstrates its successful coating. Bottom row, the coating is removed in glacial acetic acid to refresh BP surface, and then the BP is easily etched by hydrogen peroxide. The scale bars are 20 μm .

II. *n*-hexylamine/TMDs

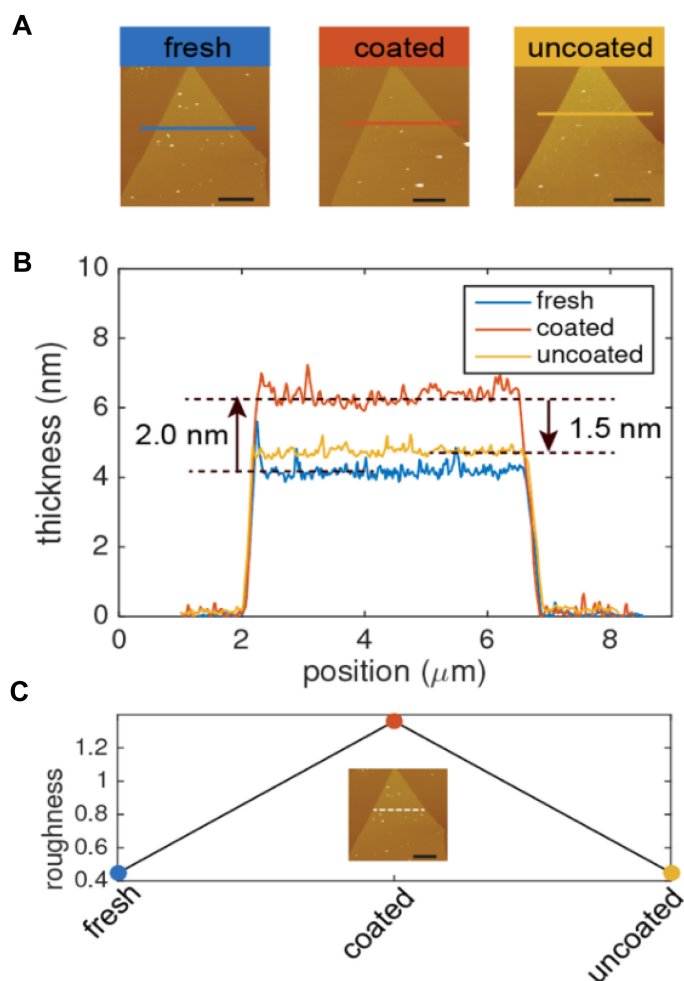


Fig. S17. Removable *n*-hexylamine coating on WSe₂. **A**, The AFM images of the same WSe₂ flake at three stages: as-exfoliated (marked as “fresh”, blue color-coded), after coating (marked as “coated”, scarlet color-coded), and after removing the coating (marked as “uncoated”, golden color-coded). **B**, The AFM characterization of the thickness of the same WSe₂ flake during three stages, with the locations of height profile marked by solid lines in **A** (Note: the same color-coding scheme was used in a-c for convenient comparison). **C**, The one-dimensional surface roughness from this WSe₂ flake during the three stages. The roughness is measured at the same location marked by white dashed line in the inset. The scale bars are 2 μm in **B** and **C**.

As the example for transition metal dichalcogenides (TMDs), WSe₂ was used to carry out a thorough removability testing by monitoring the same WSe₂ flake’s height, roughness and Raman characteristics during the three steps in treating the flake – fresh uncoated, *n*-hexylamine coated, and coating removed (fig. S17). WSe₂ flakes were exfoliated on SiO₂/Si substrate by mechanically exfoliation. The thickness of WSe₂ flakes were measured by AFM at different states (before coating hexylamine, after coating hexylamine and after removing hexylamine). To coat hexylamine, the samples were immersed in hexylamine solvent, and heat to 130 °C for 20 min. Then the sample was washed in hexane, and dry by nitrogen. To remove the hexylamine, the samples were immersed in warm acetic acid (about 50 °C) for one hour.

As shown in fig. S17C, the surface roughness of the flake is totally restored after removing the coating, and the coated *n*-hexylamine layer is 1.5 nm thick. Raman signal does not change before coating and after coating removed fig. S18. Note here, the contribution in Raman from the ultra-thin coated *n*-hexylamine layer is not observable, and hence no obvious change in Raman before and after coating for flake. However, the more significant information from Raman is that the flake property was retained from coating till coating removed, thus further consistently demonstrating our developed alkylamine monolayer coating is strong but removable.

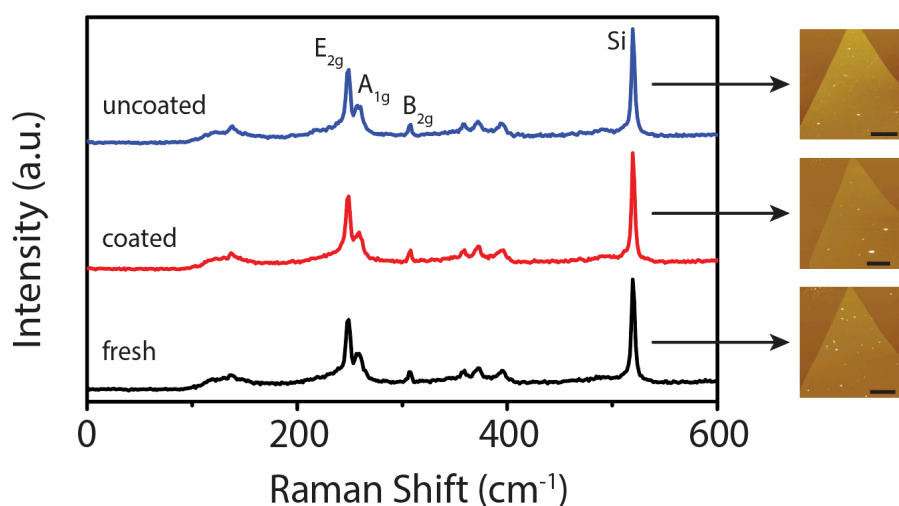


Fig. S18. Raman properties from WSe₂ during removable testing. Raman spectra taken at the same location during the three steps of removability test on *n*-hexylamine coating on the same WSe₂.

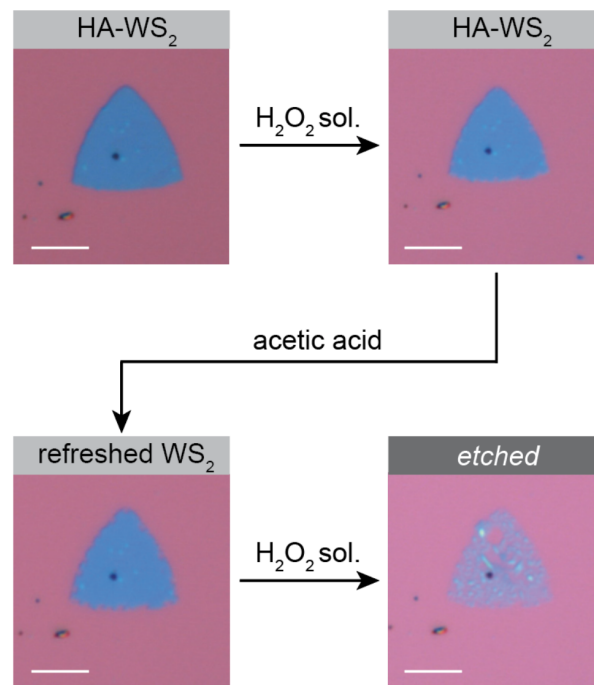


Fig. S19. Deprotection of n-hexylamine on WS₂. First row, the WS₂ has been coated with n-hexylamine and dipping inside hydrogen peroxide without etching in the center demonstrates its successful coating. Bottom row, the coating is removed in glacial acetic acid to refresh WS₂ surface, and then the WS₂ is easily etched by hydrogen peroxide. The scale bars are 20 μm.

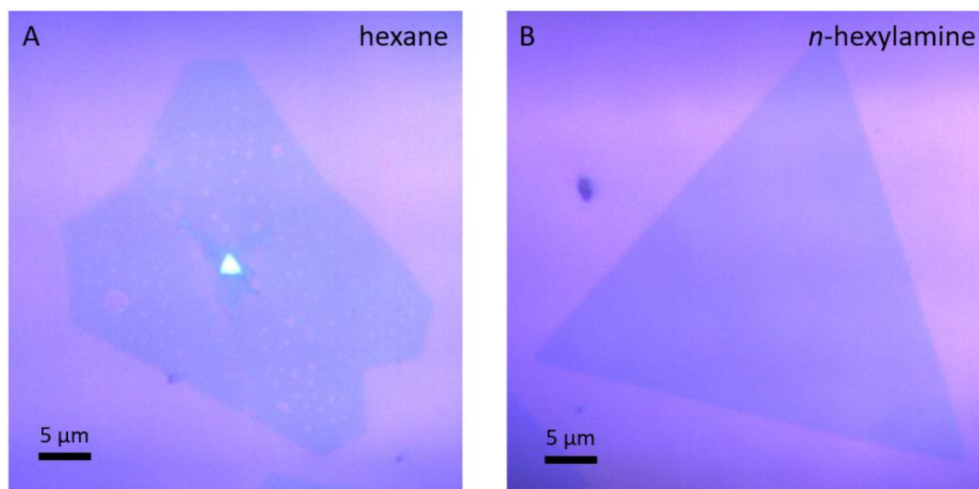


Fig. S20. A proof of the necessity of amine group (-NH₂) in protection effect. Optical images of WS₂ after applying hydrogen peroxide as etchant after coatings of (A) *n*-hexane and (B) *n*-hexylamine.

6. Protection techniques comparison

Table S4. Comparison between existing protection techniques. Factors such as coating layer thickness, resistive property, and techniques used are compared.

	Thickness	Passivation against:	Susceptible to:	Fabrication method	Limitations
<i>n</i> -hexylamine (linear alkylamine family)	~1.5 nm	Ambient air, H ₂ O ₂ , organic solvent, bases, H ₂ annealing (≥250 °C)	Organic acids	Solvothermal treatment	Size of container
AlO _x	2-30 nm	Ambient air, organic solvent	Acids, bases, H ₂ annealing	Atomic layer deposition	Scaling limited by vacuum, chamber size and processing throughput
PMMA	~100 nm	Ambient air	Organic solvent, H ₂ annealing	Spin coating	Limited spatial resolution in patterning, too thick for spacer in 2D vertical heterostructures
Graphene/hBN	~4 Å	Ambient air, organic solvent, acids, bases, H ₂ annealing	-	2D materials transfer method	Scaling limited by graphene/hBN area and transfer technique, non-removable
Parylene	30-300 nm	Ambient air	-	Thermal evaporation	Scale limited by vacuum, chamber size; processing throughput, non-removable
Aryl diazonium	Molecular scale (non specific)	Ambient air	-	Wet chemistry	Non-removable
Octadecyltrichlorosilane	Monolayer	Ambient air	-	Wet chemistry	Limited processing throughput due to its toxicity, non-removable

References

1. He, Z. *et al.* Revealing Defect-State Photoluminescence in Monolayer WS₂ by Cryogenic Laser Processing. *ACS Nano* **10**, 5847–5855 (2016).
2. Lamour, G. & Hamraoui, A. Contact Angle Measurements Using a Simplified Experimental Setup. **87**, 1403–1407 (2010).
3. Williams, D. L. *et al.* Computerised measurement of contact angles. *Galvanotechnik* **101**, 2502–2512 (2010).
4. Edmonds, M. T. *et al.* Creating a stable oxide at the surface of black phosphorus. *ACS Appl. Mater. Interfaces* **7**, 14557–14562 (2015).
5. Kresse, G. & Furthmüller, J. Efficient iterative schemes for ab initio total-energy calculations using a plane-wave basis set. *Phys. Rev. B* **54**, 11169–11186 (1996).
6. Perdew, J. P., Burke, K. & Ernzerhof, M. Generalized Gradient Approximation Made Simple. *Phys. Rev. Lett.* **77**, 3865–3868 (1996).
7. Kresse, G. From ultrasoft pseudopotentials to the projector augmented-wave method. *Phys. Rev. B* **59**, 1758–1775 (1999).
8. Grimme, S., Antony, J., Ehrlich, S. & Krieg, H. A consistent and accurate ab initio parametrization of density functional dispersion correction (DFT-D) for the 94 elements H-Pu. *J. Chem. Phys.* **132**, (2010).
9. Pack, J. D. & Monkhorst, H. J. ‘special points for Brillouin-zone integrations’-a reply. *Phys. Rev. B* **16**, 1748–1749 (1977).
10. Tang, W., Sanville, E. & Henkelman, G. A grid-based Bader analysis algorithm without lattice bias. *J. Phys. Condens. Matter* **21**, 84204 (2009).
11. Yu, M. & Trinkle, D. R. Accurate and efficient algorithm for Bader charge integration. *J. Chem. Phys.* **134**, 0–8 (2011).
12. Low, T., Engel, M., Steiner, M. & Avouris, P. Origin of photoresponse in black phosphorus phototransistors. *Phys. Rev. B - Condens. Matter Mater. Phys.* **90**, 1–5 (2014).
13. Yuan, H. *et al.* Polarization-sensitive broadband photodetector using a black phosphorus vertical p-n junction. *Nat. Nanotechnol.* **10**, 1–8 (2015).